
Master Thesis

Max Mustermann

Combining Machine-Learning and Dynamic Network Models to Improve Sepsis Prediction

January 15, 2026

supervised by:

Albert Dreistein

Wolfgang St. Pauli

Hamburg University of Technology
Institute for Biomedical Imaging
Lottestraße 55
22529 Hamburg

University Medical Center Hamburg-Eppendorf
Section for Biomedical Imaging
Martinistraße
20246 Hamburg

Hiermit erkläre ich, Author, an Eides statt, dass ich die vorliegende Masterarbeit im Studiengang Example-Program selbstständig verfasst und keine anderen als die angegebenen Hilfsmittel – insbesondere keine im Quellenverzeichnis nicht benannten Internet-Quellen – benutzt habe. Alle Stellen, die wörtlich oder sinngemäß aus Veröffentlichungen entnommen wurden, sind als solche kenntlich gemacht. Ich versichere weiterhin, dass ich die Arbeit vorher nicht in einem anderen Prüfungsverfahren eingereicht habe. Sofern im Zuge der Erstellung der vorliegenden Abschlussarbeit gKI-basierte elektronische Hilfsmittel verwendet wurden, versichere ich, dass meine eigene Leistung im Vordergrund stand und dass eine vollständige Dokumentation aller verwendeten Hilfsmittel gemäß der Guten Wissenschaftlichen Praxis vorliegt. Ich trage die Verantwortung für eventuell durch die gKI generierte fehlerhafte oder verzerrte Inhalte, fehlerhafte Referenzen, Verstöße gegen das Datenschutz- und Urheberrecht oder Plagiate.

Hamburg, den 15.01.2026

(Author)

Abstract

Contents

1. Introduction	3
2. Medical Background (Sepsis)	5
2.1. Biology of Sepsis	5
2.2. Sepsis-3 Definition	8
2.3. The need for sepsis prediction	10
3. State of the Art	13
3.1. Model-Based Approaches	13
3.2. Data-Driven Approaches	13
3.3. Challenges in comparing sepsis prediction models	14
3.4. Summary of State of the Art	15
4. Model Background (Dynamic Network Model)	17
4.1. Theoretical Background: The Kuramoto Oscillator Model	18
4.2. Description	21
4.3. Implementation	24
4.4. Limitations and Research Direction	31
4.5. Summary of the DNM	33
5. Method (Latent Dynamics Model)	35
5.1. Formalizing the Prediction Strategy	35
5.2. Architecture	38
5.3. Summary of Methods	49
6. Experiment	51
6.1. Data	51
6.2. Implementation Details	54
6.3. Evaluation Metrics	55
6.4. Results and Benchmark Comparisons	56
7. Results	57
8. Conclusion	59
A Appendix	61
A.1 SOFA - Details	61
A.2 DNM as Lie Formulation	62
A.3 Input Concepts	62
Bibliography	65

List of tables

Table 1 DNM Notation Table	22
Table 2 Simulation Parameterization	25
Table 3 Specific β - σ combinations to illustrate simulation results	28
Table 4 LDM Notation Table	39
Table 5 Training Objectives	48
Table 6 Characteristics and demographics of the cohort	53
Table 7 TODO	61
Table 8 Static input features for the prediction task	62
Table 9 Dynamic input features for the prediction task.	62

List of figures

Figure 1 Illustration and microscopic image of Stroma and Parenchymal Cells	6
Figure 2 Timings of the Sepsis-3 definition	10
Figure 3 Offline vs. Online prediction	14
Figure 4 Synchronization transition in the Kuramoto model	19
Figure 5 Schematic illustration of the Dynamic Network Model	21
Figure 6 DNM Initialization	26
Figure 7 Snapshots of simulated system states	29
Figure 8 Temporal evolution of the phase- and frequency-synchronization metrics ..	30
Figure 9 Phase Space of σ and β	31
Figure 10 Infection Indicator Module Architecture	40
Figure 11 SOFA Predictor Module Architecture	43
Figure 12 Latent Lookup	44
Figure 13 Decoder Architecture	46
Figure 14 Complete LDM Architecture	46
Figure 15 Cohort selection and exclusion process	52

Acronyms Index

ABX:	Antibiotics
AUPRC:	Area Under Precision Recall Curve
AUROC:	Area Under Receiver Operationg Curve
BCE:	Binary Cross Entropy
DAMP:	Damage-Associated Molecular Patterns
DL:	Deep Learning
DNM:	Dynamic Network Model
EHR:	Electronic Health Record
FN:	False Negatives
FP:	False Positives
FPR:	False Positive Rate
FSQ:	Finite Scalar Quantization
GPU:	Graphics Processing Unit
GRU:	Gated Recurrent Unit
ICU:	Intensive Care Unit
IQR:	Inter Quantile Range
JIT:	Just In Time Compilation
LDM:	Latent Dynamics Model
LOS:	Length Of Stay
LSTM:	Long Short-Term Memory
MIMIC:	Medical Information Mart for Intensive Care
ML:	Machine Learning
MLP:	Multi Layer Perceptron
MSE:	Mean Squared Error
ODE:	Ordinary Differential Equation
PAMP:	Pathogen-Associated Molecular Patterns
PID:	Proportional-Integral-Derivative
PINN:	Physics Informed Neural Networks
PRR:	Pattern Recognition Receptors
qSOFA:	Quick Sequential Organ Failure Assessment
RAG:	Retrieval Augmented Generation
ReLU:	Rectified Linear Unit
RNN:	Recurrent Neural Networks
SIRS:	Systemic Inflammatory Response Syndrome
SI:	Suspected Infection
SOFA:	Sequential Organ Failure Assessment
SVM:	Support Vector Machine
TN:	True Negatives
TPR:	True Positive Rate
TP:	True Positives
TUHH:	Hamburg University of Technology
YAIB:	Yet Another ICU Benchmark

- Styling level 1 header
- fix Bibliography in TOC
- fix figure captions
- pretty tables
- Sources misc + link
- Eq/fig numberings
- TUHH address wrong in template

actual functional model what is learned connecting parts

1 Introduction

2 Medical Background (Sepsis)

As the most extreme course of an infectious disease, sepsis poses a very serious health threat, with a high mortality rate and frequent long-term consequences for survivors. In 2017, an estimated 48.9 million people worldwide suffered from sepsis and the same year, 11 million deaths were associated with sepsis [1], which makes up 19.7% of yearly deaths, making it the most common cause of in-hospital deaths. Even with successful treatment, around 40% of those affected suffer long-term consequences, such as cognitive, physical or physiological problems, the so called *post-sepsis syndrome* [2]. The observed risk of mortality significantly differs between lower to middle income countries with > 50% and high income countries with < 25%. Overall, septic diseases represent an enormous burden on the global healthcare system.

Quantitatively, almost half of all sepsis-related deaths occur as a secondary complication of an underlying injury or a non-communicable, also known as chronic disease [3]. But the underlying biological triggers for sepsis as well as individual patient progressions are highly diverse and heterogeneous. Moreover, a septic condition can not be reduced to a single specific physiological phenomenon, instead it combines multiple complex and interdependent processes across different biological scales.

The following chapter is structured around the most commonly used and widely accepted sepsis definition, which is referred to as *Sepsis-3*, it characterizes sepsis as a “life-threatening organ dysfunction caused by a dysregulated host response to infection” [4]. Starting with Section 2.1, both the pathology and underlying biology of that definition are described phenomenologically. Followed by Section 2.2, which provides a more medical and technical overview to this definition. In Section 2.3 the necessity for reliable and clinically practical sepsis prediction systems is discussed and how these systems are utilized in clinical practice.

2.1. Biology of Sepsis

This part tries to give an introduction into the biological phenomena that underlie sepsis. Starting with an explanation on how human tissue is reacting to local infections or injuries on a cellular level in Section 2.1.1 and how this can escalate to *cytokine storms* in Section 2.1.2 and ending with systemic organ failure in Section 2.1.3.

Certain details and specificities are left out when not essential for the understanding of this project. More detailed explanations can be found in the primary resources provided throughout this section.

2.1.1. Cellular Origins

Human organ tissue can be differentiated into two broad cell-families called *parenchymal* and *stroma* which are separated by a thin, specialized boundary layer known as the *basal lamina*.

The parenchymal cells perform the primary physiological functions of an organ, with every organ hosting distinct parenchymal cells. For example, Cardiomyocytes in the heart drive the contraction, relaxation and therefore blood pumping, Hepatocytes in the liver doing metabolism and detoxification and Neurons in the brain providing signal transmission [5].

Everything not providing organ-specific functionalities forms the stroma, that includes the structural or connective tissue, blood vessels and nerves. The stroma not only contributes to the tissues structure, but it also actively participates in biochemical signaling and immune regulation. This way it helps to maintain a healthy and balanced tissue, the *homeostasis*, and enables coordinated responses to injury or infection [6].

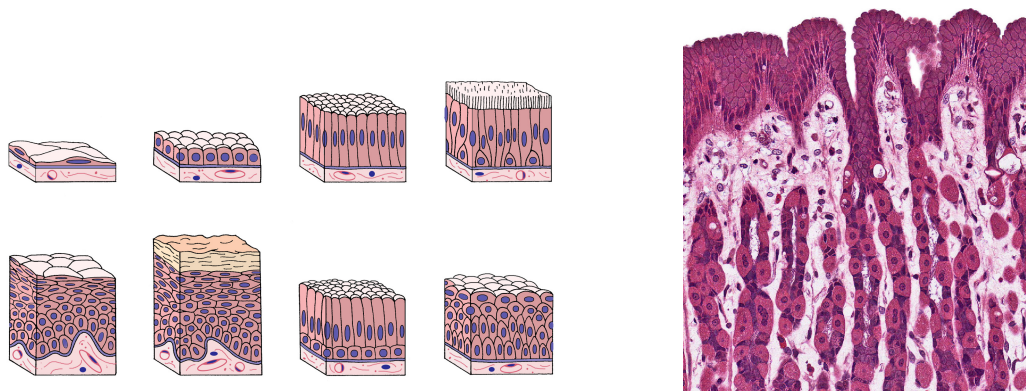


Figure 1: On the left hand side, an illustration of parenchymal cells sitting on top of the basal lamina (thin light-blue section) and the stroma in very light pinkish color building the base. The illustration shows the parenchymal cells in different shapes and organization [7]. On the right hand side a microscopic image of stomach tissue, with tightly packed parenchymal cells on the top and stroma cells as connective tissue in the light-pinkish color. The basal lamina is not visible at this level of magnification [8].

The pathogen summarizes all types of organisms that can be harmful to the body, this includes germs, fungi, algae, or parasites. When a pathogen enters the body through the skin, a mucous membrane or an open wound, the first line of nonspecific defense, the innate immune system [9], gets activated.

This rapid response does not require the body to have seen the specific pathogen before, opposed to a slower more specific and adapted immune response. Instead, the innate immune system can be triggered by sensing commonly shared features of pathogens, in case of germs known as Pathogen-Associated Molecular Patterns (PAMP), for injury called Damage-Associated Molecular Patterns (DAMP) [10]. The PAMP's and DAMP's can be detected by Pattern Recognition Receptors (PRR), which are found in resident immune cells, as well as stroma cells. Once a pathogen is detected a chain reaction inside the cell leads to the creation and release of signaling proteins called *cytokines* [11].

Cytokines are a diverse group of small signaling proteins which play a special role in the communication between other cells, both neighboring and across larger distances through the bloodstream. They are acting as molecular messengers that coordinate the recruitment of circulating immune cells and will guide them to the location of infection or injury [11].

Besides their role in immune activation where cytokines regulate the production of anti- and pro-inflammatory immune cells which help with the elimination of pathogens and trigger the healing process right after. They are also participating in the growing process of blood cells.

One specialty of these relatively simple proteins is that they can be produced by almost every other cell, with different cells being able to produce the same cytokine. Further, cytokines are redundant, meaning targeted cells can show identical responses to different cytokines [12], these features seem to fulfill some kind of safety mechanism to guarantee vital communication flow. After release cytokines have relatively a short half-life (only a few minutes) but through cascading-effects the cytokines can have substantial impact on their micro-environment.

2.1.2. Cytokine Storms

The host's dysregulated response to an infection connected to the septic condition is primarily driven by the excessive and uncontrolled release of cytokines and other mediators. Under normal circumstances, the release of inflammatory cytokines is tightly regulated in time and magnitude. After the pathogen is detected, the release of cytokines is quickly initiated. The release peaks as immune cells are recruited and automatically fades out once the initial pathogen is controlled and the host returns to a healthy and balanced state, the homeostasis.

In certain scenarios a disturbance to the regulatory mechanisms triggers positive inflammatory feedback loop, followed by a massive release of pro-inflammatory cytokines. These cells further activate additional immune and non-immune cells, which in turn amplify the cytokine production, creating a self-reinforcing cycle of immune activation [13]. This ultimately leads to a continuous and uncontrolled release of cytokines that fails to shut down. With this overreaction, called *cytokine storm*, the immune response and release of inflammatory mediators can damage the body more than the infection itself.

Although the quantity of cytokines roughly correlates with disease severity, concentrations of cytokines vary between patients, time and even different body-parts, making a distinction between an appropriate reaction and a harmful overreaction almost impossible [13]. Out of all cytokines, only a small subset or secondary markers can be measured through blood samples to detect increased cytokine activity. This limited accessibility makes cytokines difficult to study in general, they prove to be little useful as direct indicators of pathogenesis or diagnostic purposes.

Since the 90s there has been a lot of research focused on cytokines and their role in the innate immune system and overall activation behavior. Multiple therapeutic interventions have been tested in clinical trials, yet none have achieved a significant improvement in survival outcomes [10]. This emphasizes the complexity of sepsis as a systemic syndrome rather than a single-cause disease, and suggests that cytokine storms are an emergent property rather than the

result of any one molecular trigger. To this day, the fundamental principles that govern the transition from a regulated immune response to a self-destructive cytokine storm remain not fully understood.

2.1.3. Systemic Consequences and Organ Failure

While more and more cytokines are released, they flood not only infected areas, but also surrounding parts of the tissue and circulation, causing localized inflammatory response to become systemic. The widespread cytokine reaction starts to disrupt the normal metabolism of parenchymal cells in organs due to a deficiency in oxygen and nutrients.

To compensate, cells switch from their usual oxygen-based metabolism to an *anaerobic glycolysis* [14], generating energy less efficiently from glucose. As a result, metabolic by-products such as lactate accumulate making the surrounding environment more acidic, which further harms the cells and leads to more cellular dysfunction.

At the same time, the mitochondria start to fail. The walls of blood vessels become leaky, allowing fluids to move into surrounding tissue. This causes swelling and lowers the blood pressure, which in turn reduces the oxygen supply even further [10].

Step by step, the death of cells spreads throughout the body and affects organ functionality. When multiple organs fail simultaneously, the condition becomes irreversible [4]. A patient at this stage is in septic shock, the final and most deadly lethal form of sepsis, with each additional affected organ the mortality increases drastically.

2.2. Sepsis-3 Definition

As illustrated in the previous section, it is difficult to pin-point the exact moment at which the immune response switches from normal to dysregulated behavior. To classify patients at septic multiple clinically grounded definitions have been proposed over time. The most up to date and widely used definition, called Sepsis-3, will be introduced in this section. The Sepsis-3 definition as been created by a working group led by the “Society of Critical Care Medicine and the European Society of Intensive Care Medicine” in 2016. Their resolution, named “Third International Consensus Definitions for Sepsis and Septic Shock” [4], hence the name Sepsis-3, provides until today the most widely used sepsis definition and guidance on sepsis identification.

In general, sepsis does not classify as a specific illness, rather a multifaceted condition of “physiologic, pathologic, and biochemical abnormalities” [4], and septic patients are largely heterogeneous. Also the trigger is explicitly nonspecific, since different triggers can cause the same septic condition. Most commonly the underlying cause of sepsis is diarrhoeal disease, the most common underlying injury stems from road traffic injuries and maternal disorders the most common non-communicable disease causing sepsis [1].

According to the Sepsis-3 definition, a patient is in a septic condition if the following two criteria are fulfilled:

1. **Confirmed or Suspected Infection**, which has no strict medical definition or classification, meaning what counts as Suspected Infection (SI) remains a vague. Ultimately it is left for the medical personnel to classify infections or the suspicion of infections. For retrospective data-driven classification it is suggested to characterize any patient prescribed with Antibiotics (ABX) followed by the cultivation of body fluids, or the other way around, with a SI [4].

The timings of prescription and fluid samplings play a crucial role. If the antibiotics were administered first, then the cultivation has to be done in the first 24 hours after first prescription, if the cultivation happened first, the ABX have to be prescribed in the following 72 hours [4]. These timings can be seen in the lower part of Figure 2, with the abbreviated ABX. Regardless which happened first, the earlier of the two times is treated as the time of suspected infection onset time.

2. **Dysregulated Host Response** is characterized by the worsening of organ functionality over time. To measure the “amount of dysregulation” the Sepsis-3 consensus relies on the Sequential Organ Failure Assessment (SOFA)-score introduced in ([4], [15]). The score is

now regularly used to evaluate the functionality of organ systems and helps to predict the risk of mortality, also outside of a sepsis context. The SOFA score is calculated at least every 24 hours and assess six different organ systems by assigning a score from 0 (normal function) to 4 (high degree of dysfunction) to each. The overall score is calculated as sum of each individual system.

It includes the respiratory system, the coagulation/clotting of blood, i.e. changing from liquid to gel, the liver system, the cardiovascular system, the central nervous system and the renal system/kidney function. A more detailed listing of corresponding markers for each organ assessment can be found in table Table 7 in the Appendix A.1. The magnitude of a patients initial SOFA-score captures preexisting organ dysfunction. An increase in SOFA score ≥ 2 corresponds to an acute worsening of organ functionalities and a drastic worsening in the patients condition, the indicator for a dysregulated response.

The combination of the two criteria represents an exaggerated immune reaction that results in organ dysfunction, when infection is first suspected, even modest organ dysfunction is linked to a 10% increase of in-hospital mortality.

2.2.1. Sepsis Classification

The Sepsis-3 definition not only provides the clinical criteria of septic conditions, but also introduces the necessary time windows for sepsis classification. An increase of SOFA ≥ 2 in the 48 hours before or 24 hours after the SI time, the so called SI-window, is per Sepsis-3 definition the *sepsis onset time*. A schematic of the timings is shown in figure Figure 2.

With respect to which value the increase in SOFA is measured, i.e. the baseline score, is not clearly stated in the consensus and leaves room for interpretation, commonly used approaches include:

- the minimal value inside the SI-window before the SOFA increase,
- the first value of the SI-window,
- the lowest value of the 24h previous to the increase.

can we fix
please?

Differences in definitions greatly influence the detection of sepsis, which are used for prevalence estimates for example [16]. Using the lowest SOFA score as baseline, the increase ≥ 2 for patients with suspected infection was associated with an 18% higher mortality rate according to [15] a retrospective Intensive Care Unit (ICU)-data analysis.

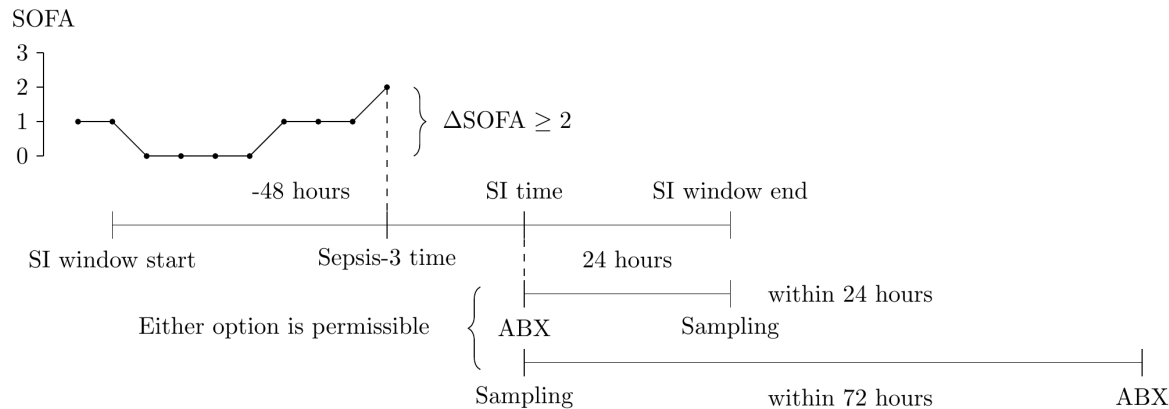


Figure 2: Graphical representation of the timings in the Sepsis-3 definition, taken from [17]

Up until today, even though SOFA was created as a clinical bedside score, some of the markers used in it are not always available to measure or at least not at every 24h [18]. For a faster bedside assessment [15] also introduced a clinical score termed Quick Sequential Organ Failure Assessment (qSOFA), with highly reduced marker number and complexity, it includes:

- Respiratory rate $\geq 22/\text{min}$
- Altered mentation
- Systolic blood pressure $\leq 100 \text{ mmHg}$

Patients fulfilling at least two of these criteria have an increased risk of organ failure. While the qSOFA has a significantly reduced complexity and is faster to assess it is not as accurate as the SOFA score, meaning it has less predictive validity for in-hospital mortality [15].

There is also the notion of a septic shock, also defined in [4], which an in-hospital mortality above 40%. Patients with a septic shock are can be identified by:

- Sepsis
- Persisting hypotension requiring vasopressors to maintain MAP $\geq 65\text{mmHg}$
- Serum lactate level $> 2 \text{ mmol/L}$, despite volume resuscitation.

2.3. The need for sepsis prediction

To this day sepsis, and the more extreme septic shock, remains an extreme burden to the worldwide healthcare system. It is associated with high rates of incidence, high mortality and significant morbidity. Despite overall advancements in medical care and slowly decreasing prevalence numbers, sepsis continues to be the leading cause of in-hospital death [19].

In Germany it was estimated in 2022 that at least 17.9% of intensive care patients develop sepsis, and 41.7% of all hospital treated sepsis patients die during their stay [3]. The economic

burden is equally severe, with the annual cost of sepsis treatment in Germany estimated to be €7.7 billion based on extrapolated data from 2013 [3].

Globally sepsis remains to be under-diagnosed significantly due to its nonspecific symptoms. Environmental and socioeconomic factors, such as insufficient sanitation, limited access to clean water and healthcare increase the incidence particularly in low- to middle income countries [1], [19].

In the past two decades, through an increasing availability and usage of Electronic Health Record (EHR) in hospitals, automated patient monitoring systems have become more prominent. These systems are designed to alert medical personnel to confirmed or suspected sepsis, as well as to elevated sepsis risk, based on predetermined criteria which are derived from continuously collecting clinical and laboratory measurements. With the help of these automated alerts, clinicians can potentially more rapidly initiate antibiotic or other treatment or intensify patient monitoring.

A meta-analysis of seven sepsis alert systems found no evidence for improvement in patient outcomes, suggesting insufficient predictive power of analyzed alert systems or inadequate system integration [20]. Nevertheless, positive treatment outcomes depend heavily on timely recognition and intervention [19]. Each hour of delayed treatment increases mortality risk, underscoring the critical importance of early detection [21] while structured screening and early warning systems have demonstrated reductions in time-to-antibiotics and improvements in outcomes [22]. These findings confirm that earlier identification of sepsis improves clinical results, even if existing tools are not yet capable enough, and emphasize the need for developing more reliable alert systems.

A recent study suggests a paradigm shift in sepsis detection, namely from a purely symptom-based to a systems-based approach [23]. Instead of waiting for clinical signs, i.e. symptoms, early recognition should integrate multiple physiological and biochemical signals to capture the transition from infection to organ dysfunction. This aligns with the findings of a survey among clinicians regarding Artificial-Intelligence-Assistance in healthcare [24]. According to the survey, one participant emphasizes that specific vitals signs might be of less importance, rather the trend of a patient's trajectory itself should be the prediction target. Another finding of the same study was the preference of trajectories over plain binary event predictions.

Despite these promising directions, the translation of predictive models into clinical practice has proven challenging. Studies consistently identify barriers, such as alert fatigue, where excessive false positives or clinically non-actionable alarms disrupt workflow, reduce clinician trust, and ultimately lead to ignored warnings. Prediction systems face a fundamental trade-off: higher sensitivity captures more true cases but generates more false alarms, while higher specificity reduces alert fatigue but risks missing sepsis cases where early treatment is critical. To be effective, predictive systems must integrate seamlessly into existing workflows provide interpretable output and support clinical expertise [24].

Taken together, these insights highlight both the need and the opportunity for improved sepsis prediction. The global burden and clinical urgency justify the development of more reliable prediction systems. At the same time, the limitations of current alert systems and

implementation barriers underline the necessity for models that can integrate dynamic patient data and capture clinical trajectories. The following chapter examines existing approaches to sepsis prediction and identifies key gaps that motivate the present work.

3 State of the Art

This chapter provides a brief overview of the current state of the art in automated sepsis prediction and concludes in Section 3.3 with some fundamental challenges found when assessing sepsis prediction systems. Sepsis prediction models for individual patients can be categorized into two major classes, the model-based and the data-driven approaches.

3.1. Model-Based Approaches

Biological and medical inspired models of sepsis offer high interpretability and explainability, since they explicitly encode causal relationships. However, due to the inherent complexity of sepsis pathophysiology, such mechanistic models remain rare [25]. Most existing works focus on dynamic immune response on a cellular [26], [27], [28], [29], intricate signaling and production mechanisms influenced by varying cell concentration are typically modeled using large systems of coupled differential equations.

To derive risk estimates or disease trajectories, model parameters are fitted to individual patient observations. By simulating physiological trajectories under hypothetical infection scenarios, these models enable to estimate the likelihood of sepsis development [27]. More advanced digital twins which incorporate bidirectional feedback between the mechanistic model and patient data have also been explored in [28].

Validation mechanistic sepsis models is usually done by comparing simulation trajectories to repetitively measured cellular concentrations. Since the required high-resolution immunological measurements are difficult and costly to obtain only small samples of patients have been validated. To date no model-based prediction approaches has yet been evaluated on large-scale clinical datasets, limiting their insight into real-world performance and generalizability.

3.2. Data-Driven Approaches

With the increasing availability of Electronic Health Record and computational resources, Machine Learning (ML)- and Deep Learning (DL)-methods have become the dominant paradigm for sepsis prediction systems over the last decade. Data-driven approaches can capture highly nonlinear relationships in heterogeneous clinical data and have demonstrated strong empirical performance in real-world settings. Numerous systems have been proposed

and are summarized in surveys such as [30] and [31]. The technology-landscape is highly diverse and includes classical ML-models (nonlinear regression, random-forests, Support Vector Machine (SVM)s, and gradient-boosted trees such as XGBoost [32]), as well as DL-architectures (standard Multi Layer Perceptron (MLP), recurrent models e.g. Gated Recurrent Unit (GRU)/Long Short-Term Memory (LSTM), attention based e.g. transformers and more specialized models like Gaussian Process Temporal Convolutional Networks [33]).

3.3. Challenges in comparing sepsis prediction models

Although many of data-driven models report reasonable performance, direct comparison across studies is fundamentally limited, as highlighted by [31]. The main issues particularly relevant to the Latent Dynamics Model (LDM) methodology are:

- **Prediction Tasks**

Studies differ fundamentally in how they frame the prediction problem. This includes *online training*, where newly arriving medical measurements are incorporated into a continuously updated risk estimate and *offline training*, where only the information available at a fixed observation time is used to predict the risk of sepsis within a prespecified horizon T . Because these setups rely on different information structures and temporal assumptions, their reported performances are not directly comparable. Online prediction is more clinically desirable but also more challenging to implement given the current state of available EHR. Both schemes are shown in Figure 3, notice in offline prediction the horizon T , the specific choice strongly influences the outcome, with smaller horizons the tasks becomes gradually easier. For the online scheme choice of what time range around a sepsis onset qualifies as positive label also significantly changes prediction accuracy and prediction.

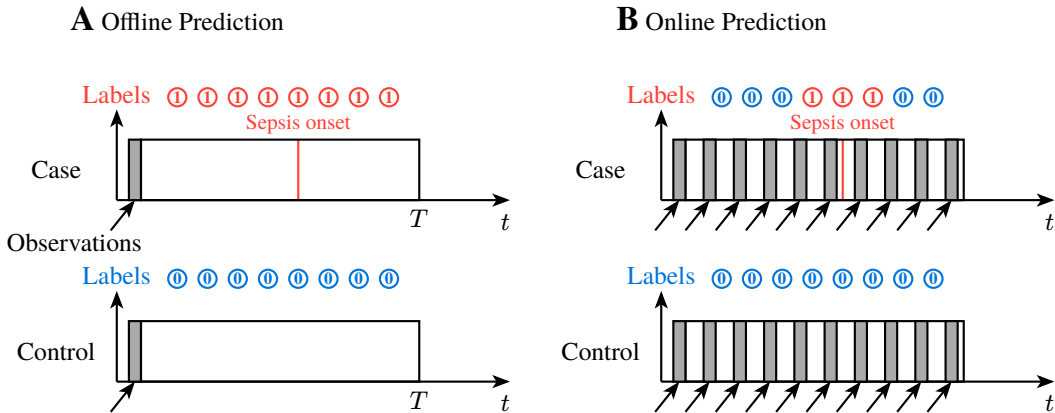


Figure 3: Illustration of the two predictions schemes, *offline* (A) vs. *online* (B) (figure heavily inspired by [31]). The main difference is the provision and utilization and arrival of observation data.

To have a meaningful comparisons between two models, they must be evaluated on the *exact same task*. This includes the scheme (offline or online), the same choice of T for the offline scheme and the labeling window around the measured onset.

- **Sepsis Definition and Implementation**

Sepsis definitions are vary widely across studies but greatly influence the prevalence, cohort composition as well as task difficulty. Intuitively different sepsis different sepsis definitions are not comparable with each other since they might capture dissimilar medical concepts. Even for the same conceptual definition and same dataset differences in implementation can yield different patient cohorts and therefore different prediction performances [16]. More restrictive definitions typically produce lower prevalence and greater class imbalances making ML-based prediction more difficult but potentially increasing clinical relevance. Less restrictive definitions can artificially inflate prediction performance while reducing practical applicability.

- **Feature selection**

Feature choice also influences both model performance and real-world usability. Using a broader set of features can increase predictive accuracy but risks again the clinical applicability, since extensive measurements may be not routinely available. It also increases the risk of label leakage, where the measurements and medical concepts used to derive the sepsis label are provided to the prediction model as feature input. This way the model would learn the sepsis derivation but not underlying signals which are actually helpful for early sepsis recognition.

3.4. Summary of State of the Art

As of now, neither purely model-based nor purely data-driven approaches were able to fully address the challenges of sepsis prediction. Mechanistic models offer strong interpretability and encode physiological priors, yet their practical usefulness is limited by the scarcity of high-resolution immunological measurements and the lack of large-scale clinical validation. In contrast, data-driven models show strong empirical performance on EHR datasets, but their prediction behavior is often difficult to interpret and show black-box behavior

This work, named the Latent Dynamics Model aims to combine the strengths of both paradigms: mechanistic components of the Dynamic Network Model (DNM) introduce structured physiological biases that can help stabilize the learning process, and provide more interpretable intermediate quantities. At the same time, the data-driven components allow the model to adapt to real clinical variability and make use of information that is not explicitly captured by the mechanistic structure. In this way, the LDM seeks to make data-driven sepsis prediction models more transparent and more robust to the well-known issues discussed in Section 3.3.

The heterogeneity in prediction tasks, sepsis definitions and feature sets illustrates why each decision of one of these aspects regarding new prediction models should be taken with care. For the sake of reproducibility the choices need to be reported as precisely as possible. Works such as Yet Another ICU Benchmark (YAIB) [34] attempt to address these challenges by

providing a common basis for evaluating models by standardizing the dataset, cohort definition, prediction task, and labeling strategy, thereby enabling fair and reproducible comparison of different approaches.

After introducing the methodology in Section 5, its performance validated on real clinical data in Section 6. The experimental setup makes use of the YAIB framework, and its dataset, cohort definition, prediction task, and labeling implementation are described in detail in Section 6.1, as these settings are adopted for training and evaluating the LDM.

4 Model Background (Dynamic Network Model)

As outlined in Section 2, the macroscopic multi-organ failure associated with sepsis is driven by a dysregulated cascade of signaling processes on a microscopic level (see Section 2.1). This cascade involves a massive amount of interconnected components, where the connections mechanics and strengths vary over time and space. For example, these interactions differ across tissues and evolve as sepsis progresses, with crossing biochemical thresholds the behavior of cells can be changed [35].

In essence, cell-to-cell and cell-to-organ interaction in septic conditions form a highly dynamic, nonlinear and spatio-temporal network of relationships [25], which cannot be fully understood by a reduction to single time-point analyzes. Even though many individual elements of the inflammatory response are well characterized, we still fail to integrate them into a coherent system-level picture.

To address this complexity, the emerging field of *Network Physiology* provides a promising conceptual framework. Rather than studying components in isolation, network physiology focuses on the coordination and interconnection among the diverse organ systems and subsystems [36]. It enables the study of human physiology as a complex, integrated system, where emergent macroscopic dynamics arise from interacting subsystems that cannot be explained by their individual behavior. This perspective translates to the mesoscopic level, i.e. the in-between of things, where the coupling mechanisms collectively determine the overall physiological function.

In network physiology, the analytical basis of the bodies interacting systems is often graph based. Nodes represent subsystem such as organs or cell populations and links represent functional couplings or communication pathways [36]. Unlike classical graph theory, where dynamics are introduced by changing the graph topology (e.g. adding or removing links or nodes), in *Complex Networks* the links themselves can evolve dynamically in response to other system variables. These adaptive connections allow for information to propagate through the whole network, giving rise to emerging phenomena on global scales for otherwise identical network topologies.

Complex networks are well studied in physics and biology and have been applied to various physiological domains. Early works, such as [37] that have studied the cardiovascular system, while more recent studies have focused on the cardio-respiratory coupling [38] and large-scale brain network dynamics [39]. Network approaches have also provided mechanistic insights into disease dynamics, for example Parkinson [40] and Epilepsy [41].

Building on these interaction centric principles has opened up new opportunities to study how the inflammatory processes, such as those underlying sepsis, emerge from the complex inter- and intra-organ communication. In particular Sawicki et. al [42] and Berner et. al [43] have introduced a dynamical system that models the cytokine behavior in patients with sepsis and cancer. This functional model will be referred to as Dynamic Network Model and forms the conceptual foundation for this whole project.

The remainder of this chapter is structured as follows: In Section 4.1 introduces the theoretical backbone of the DNM, the Kuramoto oscillator model, which provides a minimal description of synchronization phenomena in complex systems. Section 4.2 presents the formal mathematical definition of the DNM and its medical interpretation, followed by implementation details in Section 4.3 and a presentation of selected simulation results in Section 4.3.4.

4.1. Theoretical Background: The Kuramoto Oscillator Model

To mathematically describe natural or technological phenomena, *coupled oscillators* have proven to be a useful framework, for example, to model the relative timing of neural spiking, reaction rates of chemical systems or dynamics of epidemics [44]. In these cases complex networks of coupled oscillators are often capable of bridging microscopic dynamics and macroscopic synchronization phenomena observed in biological systems.

One of the most influential system of coupled oscillators is the *Kuramoto Phase Oscillator Model*. This system of coupled Ordinary Differential Equation (ODE), where each term describes an oscillator rotating around the unit circle, is often used to study how synchronization emerges from simple coupling rules. In the simplest form, it consists of $N \in \mathbb{N}_{>0}$ identical, fully connected and coupled oscillators with phase $\varphi_i \in [0, 2\pi)$, for $i \in 1 \dots N$ and an intrinsic frequency $\omega_i \in \mathbb{R}$ [45]. The phase φ_i represents the angular position on the unit circle, hence it is defined modulo 2π . The dynamics are given by the ODE system:

$$\dot{\varphi}_i = \omega_i - \frac{K}{N} \sum_{j=1}^N \sin(\varphi_i - \varphi_j) \quad (4.1)$$

Here, the $\dot{\varphi}$ is used as shorthand notation for the time derivative of the phase $\frac{d\varphi}{dt}$, the instantaneous phase velocity. An additional parameter is the global coupling strength $K \in \mathbb{R}_{>0}$ between oscillators i and $j \in 1 \dots N$. The system evolution depends on the choice of initial phases $\varphi_i(t=0)$, which are typically drawn from a uniform random distribution over $[0, 2\pi)$.

When evolving this system with time, commonly by numerical integration, since analytical solutions only exist for special cases, oscillator i 's phase velocity depends on each other oscillator j . The sine coupling $\sin(\varphi_i - \varphi_j)$ implements a phase-cohesion mechanism: oscillator i decelerates when it leads oscillator j ($0 < \varphi_i - \varphi_j < \pi$) and accelerates when it lags behind ($-\pi < \varphi_i - \varphi_j < 0$), pulling the population towards synchronization.

For sufficiently large N the oscillator population can converge towards system-scale states of coherence or incoherence based on the choice of K [46]. Coherent in this case means oscillators synchronize with each other, so they share the same phase and phase velocity,

incoherence on the other hand is the absence of synchronization (desynchronized), see Figure 4. Synchronous states can be reached if the coupling is stronger than a certain threshold $K > K_c$, the critical coupling strength [46]. In between these two regimes there is a transition-phase of partial synchronization, where some oscillators phase- and frequency-lock and others do not. The model captures the mechanism of self-synchronization, and a collective transition from disorder to order, that underlies many real world processes, which is the reason the model has attracted so much research [44].

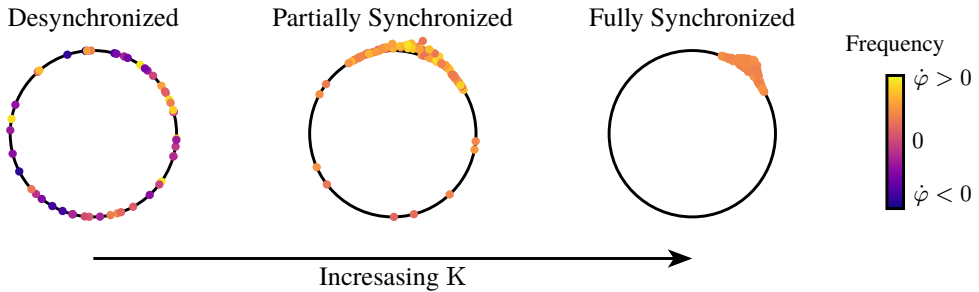


Figure 4: Illustration of the collective dynamics of a population of phase oscillators on the unit circle as the global coupling strength K is increased. Each point represents an oscillator at phase φ_i , color encodes the instantaneous phase velocity $\dot{\varphi}_i$ (blue/yellow: faster, green: slower). For weak coupling (left), oscillators are desynchronized, with phases distributed around the circle and heterogeneous frequencies. At intermediate coupling (center), partial synchronization emerges: a subset of oscillators forms a coherent cluster that phase- and frequency-locks, while the remaining oscillators drift incoherently. For sufficiently strong coupling (right), the population becomes fully synchronized, with all oscillators sharing a common phase and frequency.

4.1.1. Extensions to the Kuramoto Model

To increase the generalization ability of the system, various extensions of the basic Kuramoto model have been proposed and studied numerically and analytically. Several extensions are directly relevant to the DNM and their definitions and effects on synchronization will be introduced, with additional terms being indicated by the red color:

Phase Lag α introduced in [47], where $|\alpha| < \frac{\pi}{2}$. By shifting the coupling function, values of $\alpha \neq 0$ act as an inhibitor of synchronization, so the coupling does not vanish even when the phases align:

$$\dot{\varphi}_i = \omega_i - \frac{K}{N} \sum_{j=1}^N \sin(\varphi_i - \varphi_j + \textcolor{red}{\alpha}) \quad (4.2)$$

As a result the critical coupling strength K_c increases with α [47].

Adaptive coupling $\mathbf{K} \in [-1, 1]^{N \times N}$ moves from a global coupling strength K for all oscillator pairs to an adaptive asymmetric coupling strength for each individual pair $\mathbf{K} = (\kappa_{ij})_{(i,j) \in N \times N}$:

newpage?

$$\dot{\varphi}_i = \omega_i - \frac{1}{N} \sum_{j=1}^N \kappa_{ij} \sin(\varphi_i - \varphi_j) \quad (4.3)$$

$$\dot{\kappa}_{ij} = -\varepsilon (\kappa_{ij} + \sin(\varphi_i - \varphi_j + \beta^\mu)) \quad (4.3)$$

Here adaption rate $0 < \varepsilon \ll 1$ separates the fast moving oscillator dynamics from slower moving coupling adaptivity [48]. Such adaptive couplings have been used to model neural plasticity and learning-like processes in physiological systems [49]. The so called new phase lag parameter β of the adaptation function (also called plasticity rule) plays an essential role in the synchronization process. At a value of $\beta^\mu = \frac{\pi}{2}$ the coupling, and therefore the adaptivity, is at a maximum positive feedback, strengthening the link κ_{ij} and encouraging synchronization between oscillators i and j . This maximal connectivity is referred to *Hebbian Rule* and found in synchronizing systems such as the brain [48]. For other values $\beta^\mu \neq \frac{\pi}{2}$ the feedback is delayed $\varphi_i^\mu - \varphi_j^\nu = \beta^\mu - \frac{\pi}{2}$ by a phase lag, a value of $\beta^\mu = -\frac{\pi}{2}$ we get an anti-Hebbian rule which inhibits synchronization.

Multiplex Networks represent systems with multiple interacting layers. Multiplexing introduces a way to couple $L \in \mathbb{N}_{>1}$ Kuramoto networks (indexed by $\mu = 1, \dots, L$ and $\nu = 1, \dots, L \neq \mu$) via interlayer links:

$$\dot{\varphi}_i^\mu = \omega_i - \frac{K}{N} \sum_{j=1}^N \sin(\varphi_i - \varphi_j + \alpha^\mu) - \sigma^{\mu\nu} \sum_{\nu=1, \nu \neq \mu}^L \sin(\varphi_i^\mu - \varphi_i^\nu + \alpha^{\mu\nu}) \quad (4.4)$$

Here μ and ν represent distinct subsystems, and are connected via interlayer coupling weights $\sigma^{\mu\nu} \in \mathbb{R}_{\geq 0}$, where oscillators are acting one-to-one.

These extensions combined serve as the source of dynamics for the DNM and give rise to more intricate system states than the straightforward synchronization in the base model. Even for single layers, non-multiplexed but phase-lagged and adaptively coupled oscillators, one can observe several distinct system states, neither fully synchronized or desynchronized such as phase and frequency-clusters, chimera- and splay states. The emergence of these states depends on the choice of the coupling strength K and the phase-lag parameters α and β .

In the frequency clustered state, the oscillator phases do not synchronize, but several oscillator groups can form that share a common frequency. For the phase-clustered case, the groups additionally synchronize their phase. Frequency clusters often emerge as intermediate regimes between full synchronization and incoherence [50].

Chimera states, a special type of partial synchronization, occur when only a subset of oscillators synchronizes in phase and frequency, while others remain desynchronized. In contrast to “normal” partial synchronization they occur when the coupling symmetry breaks. In splay states, all oscillators synchronize their frequencies but do not their phases, they instead uniformly distribute around the unit circle [48].

The introduction changes the system behavior once more, for example single layers of a multiplexed system can result in the multi-clustered regime for parameters they would not in the monoplexed case. In multiplexed systems it is also possible connected layers end up in different stable state, for example, one in a clustered the other in a splay state.

4.2. Description

The DNM is a **functional** model, that means it **does not try to model things accurately on any cellular, biochemical, or organ level**, it instead tries to model dynamic interactions. At the core, the model does differentiate between two broad classes of cells, introduced in Section 2.1.1, the stroma and the parenchymal cells. It also includes the cell interaction through cytokine proteins and an information flow through the basal membrane. Importantly, the model only handles the case of already infected subjects and tries to grasp if the patients state is prone to a dysregulated host response.

Cells of one type are aggregated into layers, everything associated with parenchymal cells is indicated with an $.^1$ superscript and is called the *organ layer*, stroma cells are indicated with $.^2$ and is referred to as nonspecific *immune layer*. Each layer consists of N phase oscillators $\varphi_i^{1,2} \in [0, 2\pi]$. To emphasize again the function aspect of the model: individual oscillators do not correspond to single cells, rather the layer as a whole is associated with the overall state of all organs or immune system functionality respectively. An illustration of the biological and functional model is shown in Figure 5.

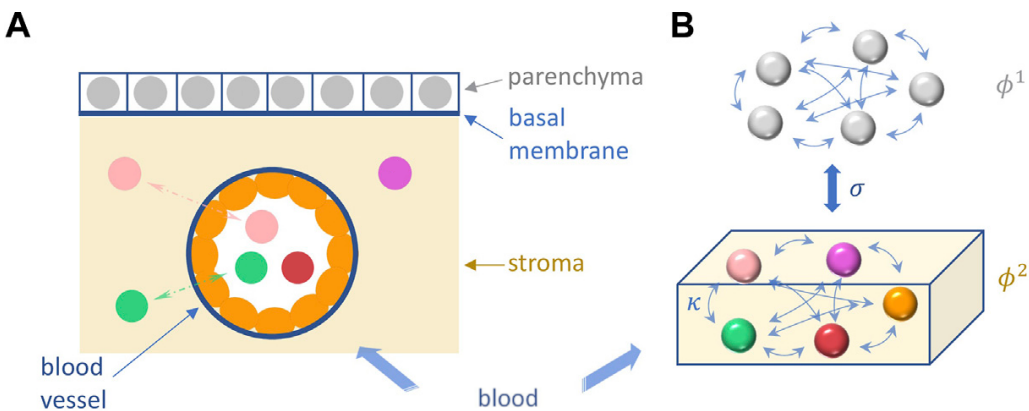


Figure 5: Image taken from [43] in a simplified form, illustrating the Dynamic Network Model. (A) A tissue element is depicted, in which the basic processes of sepsis take place. Shown are different immune and structural cells involved (colored) in the stroma (yellow area), the parenchyma (grey), and the capillary blood vessel, where cytokines, PAMPs and DAMPs are transmitted. (B) Depicts the functional interactions within and between the two corresponding network layers in the DNM, the parenchyma and the stroma (immune layer).

The metabolic cell activity is modeled by rotational velocity $\dot{\varphi}$ of the oscillators, the faster the rotation, the faster the metabolism. Each layer is fully coupled via an adaptive possibly asymmetric matrix $\mathbf{K}^{1,2} \in [-1, 1]^{N \times N}$ with elements $\kappa_{ij}^{1,2}$, these couplings represent the activity of cytokine mediation. Small absolute coupling values indicate a low communication via cytokines and grows with larger coupling strength. For the organ layer there is an additional non-adaptive coupling part $\mathbf{A}^1 \in [0, 1]^{N \times N}$ with elements a_{ij}^1 , representing a fixed connectivity within an organ.

The dimensionless system dynamics are described with the following coupled ODE terms, build on the classical Kuramoto model described in Section 4.1 and its extensions from Section 4.1.1:

$$\dot{\varphi}_i^1 = \omega^1 - \frac{1}{N} \sum_{j=1}^N \{ (a_{ij}^1 + \kappa_{ij}^1) \sin(\varphi_i^1 - \varphi_j^1 + \alpha^{11}) \} - \sigma \sin(\varphi_i^1 - \varphi_i^2 + \alpha^{12}) \quad (4.5)$$

$$\dot{\kappa}_{ij}^1 = -\varepsilon^1 (\kappa_{ij}^1 + \sin(\varphi_i^1 - \varphi_j^1 - \beta)) \quad (4.5)$$

$$\dot{\varphi}_i^2 = \omega^2 - \frac{1}{N} \sum_{j=1}^N \{ \kappa_{ij}^2 \sin(\varphi_i^2 - \varphi_j^2 + \alpha^{22}) \} - \sigma \sin(\varphi_i^2 - \varphi_i^1 + \alpha^{21}) \quad (4.5)$$

$$\dot{\kappa}_{ij}^2 = -\varepsilon^2 (\kappa_{ij}^2 + \sin(\varphi_i^2 - \varphi_j^2 - \beta)) \quad (4.5)$$

Where the interlayer coupling, i.e. a symmetric information through the basal lamina, is modeled by the parameter $\sigma \in \mathbb{R}_{\geq 0}$. The internal oscillator frequencies are modeled by the parameters $\omega^{1,2}$ and correspond to a natural metabolic activity.

Besides the coupling weights in $\mathbf{K}^{1,2}$ the intralayer interactions also depend on the phase lag parameters α^{11} and α^{22} modeling cellular reaction delay. To separate the fast moving oscillator dynamics from the slower moving coupling weights adaption rates $0 < \varepsilon \ll 1$ are introduced. Since the adaption of parenchymal cytokine communication is assumed to be slower than the immune counterpart [42], it is chosen $\varepsilon^1 \ll \varepsilon^2 \ll 1$, which introduces dynamics on multiple timescales.

Lastly, the most influential parameter is β which controls they adaptivity of the cytokines. Because β has such a big influence on the model dynamics it is called the (*biological*) *age parameter* and summarizes multiple physiological concepts such as age, inflammatory baselines, adiposity, pre-existing illness, physical inactivity, nutritional influences and other common risk factors [43].

All the systems variables and parameters are summarized in Table 1 together with their medical interpretation.

Table 1: Summarization of notation used in the Dynamic Network Model. Superscripts indicating the layer are left out for readability.

SYMBOL	NAME	PHYSIOLOGICAL MEANING
Variables		
φ_i	Phase	Group of cells
$\dot{\varphi}_i$	Phase Velocity	Metabolic activity
κ_{ij}	Coupling Weight	Cytokine activity
Parameters		
α	Phase lag	Metabolic interaction delay
β	Plasticity rule	Combined of risk factors

SYMBOL	NAME	PHYSIOLOGICAL MEANING
ω	Natural frequency	Natural cellular metabolism
ε	Time scale ratios	Temporal scale of cytokine activity
a_{ij}	Connectivity	Fixed intra-organ cell-to-cell interaction
σ	Interlayer coupling	Interaction between parenchymal and immune cells through the basal lamina
Measures		
s	Standard deviation of frequency (see Equation (4.11))	Pathogenicity (Parenchymal Layer)

4.2.1. Pathology in the DNM

A biological organism, such as the human body, can be regarded as a self-regulating system that, under healthy conditions, maintains a homeostatic state [6]. Homeostasis refers to a dynamic but balanced equilibrium in which the physiological subsystems continuously interact to sustain stability despite external perturbations. In the context of the DNM, this equilibrium is represented by a synchronous regime of both layers in the duplex oscillator system. In synchronous states, the organ layer and immune layer exhibit coordinated phase and frequency dynamics, reflecting balanced communication, collective frequency of cellular metabolism and stable systemic function.

Pathology, in contrast, is modeled by the breakdown of the synchronicity and the formation of frequency clusters in the parenchymal layer, i.e. loss of homeostatic balance. In the DNM least one cluster will exhibit increased frequency and one with lower or unchanged frequency. This aligns with medical observation, where unhealthy parenchymal cells change to a less efficient anaerobic glycosis based metabolism, forcing them to increase their metabolic activity to keep up with the energy demand. Remaining healthy cells are expected to stay frequency synchronized to a lower and “healthy” frequency.

There are two more cases, neither fully healthy nor fully pathologic, representing a vulnerable or resilient patient condition. The healthy but vulnerable case corresponds to a splay state, where phases in the parenchymal layer are not synchronized, but the frequencies are, weakening the overall coherence [43]. A resilient state corresponds to cases where both the phase and frequency of the parenchymal layer are synchronized, but the immune layer exhibits both frequency and phase clustering.

It is important to note, that the ODE dynamics or system variable trajectories **do not** translate to the evolution of a patients pathological state. Instead, the amount of desynchronization of the parenchymal layer when reaching a steady system state can be interpreted as the current state of a patients organ functionality. The “result” or solution of the coupled oscillator system does not provide any temporal insights, but only describe the current condition. Time-steps taken inside the model cannot be compared to any real-world time quantity.

4.3. Implementation

This subsection describes the implementation for the numerical integration of the DNM defined in Equation (4.5), the choice of initial parameter values and how (de-)synchronicity/disease severity is quantified. One goal of this implementation is to partly reproduce the numerical results presented in [43], since they will be serving as a basis for following chapters.

4.3.1. Implementation Details

The backbone for the present numerical integration is JAX [51], a Python package for high-performance array computation, similar to NumPy or MATLAB but designed for automatic differentiation, vectorization and Just In Time Compilation (JIT). JIT-compilation and vectorization allow high-level numerical code to be translated to highly optimized accelerator-specific machine code, for example Graphics Processing Unit (GPU). This way, performance benefits of massively parallel hardware can be utilized with minimal extra programming cost. For the actual integration a differential equation solver from diffrax [52] was used, which provides multiple solving schemes fully built on top of JAX.

While [43] uses a fourth-order Runge-Kutta method and a fixed step-size, this implementation¹ uses the Tsitouras 5/4 Runge-Kutta method [53] with adaptive step-sizing controlled by a Proportional-Integral-Derivative (PID) controller, allowing for more efficient integration while keeping similar accuracy. A relative tolerance of 10^{-3} and an absolute tolerance 10^{-6} were chosen. All simulations were carried out in 64-bit floating point precision, necessary for accurate and stable system integration.

Because of the element-wise differences used in the coupling terms $\varphi_i^{1,2} - \varphi_j^{1,2} \in \mathbb{R}^{N \times N}$ the computational cost scales quadratically with the number of oscillators N . These differences are then transformed by the computationally expensive trigonometric sin routine. To accelerate integration, these trigonometric evaluations were optimized following [54]. Terms in the form $\sin(\theta_l - \theta_m)$ were expanded as:

$$\sin(\theta_l - \theta_m) = \sin(\theta_l) \cos(\theta_m) - \cos(\theta_l) \sin(\theta_m) \quad \forall l, m \in \{1, \dots, N\} \quad (4.6)$$

By caching the terms $\sin(\theta_l)$, $\sin(\theta_m)$, $\cos(\theta_l)$, $\cos(\theta_m)$ once per iteration, the number of trigonometric evaluations per iteration is reduced from $2 \cdot [N(N - 1)]$ to $2 \cdot [4N]$, significantly improving performance for mid to large oscillator populations.

Additionally, an alternative implementation based on Lie-algebra formulations was also explored, utilizing their natural representation for rotations in N-D-space. Although theoretically promising in terms of numerical accuracy and integration stability, this approach did not yield practical advantages in performance. Further details on this reformulation are provided in Appendix A.2.

[schreiben](#)

¹The code is available at https://github.com/unartig/sepsis_osc/tree/main/src/sepsis_osc/dnm

4.3.2. Parameterization and Initialization

The DNM is dimensionless and not bound to any physical scale, that means there is no medical ground truth of parameter values and their choice is somewhat arbitrary. For the present implementation the parameterization is adopted from the original works [42] and [43] since they have already shown desired properties of (de-)synchronization and valid medical interpretations for these parameter choices.

The majority of their parameter choices heavily simplify the model. First of all, the different natural frequencies are treated as equal and are set to 0 giving $\omega^1 = \omega^2 = \omega = 0$, any other choice of ω just changes the frame of reference (co-rotating frame), the dynamics stay unchanged [43]. The phase lag parameters for the inter layer coupling are both set to $\alpha^{12} = \alpha^{21} = 0$, yielding instantaneous interactions, the intralayer phase lags are set to $\alpha^{11} = \alpha^{22} = -0.28\pi$, which was the prominently used configuration in [43] yielding the desired dynamical properties. The constant intralayer coupling in the parenchymal is chosen as global coupling $a_{ij} = 1$ if $i \neq j$ else 0.

The adaptation rates are chosen as $\varepsilon^1 = 0.03$ and $\varepsilon^2 = 0.3$, creating the two dynamical timescales for slow parenchymal and faster immune cells. The number of oscillators per layer is chosen as $N = 200$ throughout all simulations. To account for the randomly initialized variables, each parameter configuration is integrated for an ensemble of $M = 50$ initializations. This randomization of initial values is used to account for epistemic uncertainties, i.e. systemic errors introduced by modeling simplifications.

In [43] the influence of parameter values for β and σ was investigated and not constant throughout different simulations, with $\beta \in [0.4\pi, 0.7\pi]$ and $\sigma \in [0, 1.5]$, in this work the interval for β was increased to $[0.0, 1.0\pi]$. An exhaustive summary of all variable initializations and parameter choices can be found in Table 2.

Table 2: Parameterization and initialization of the DNM used for the numerical integration.

SYMBOL	VALUE	SYMBOL	VALUE
Variables			
φ_i^1	$\sim \mathcal{U}[0, 2\pi)$	$\kappa_{i \neq j}^1$	$\sim \mathcal{U}(-1, 1)$
φ_i^2	$\sim \mathcal{U}[0, 2\pi)$	$\kappa_{i \neq j}^2$	clusters of size C and $1 - C$
Parameters			
M	50	N	200
C	20%		
β	$[0.0, 1.0]\pi$	σ	$[0.0, 1.5]$
α^{11}, α^{22}	-0.28π	α^{12}, α^{21}	0.0
ω_1, ω_2	0.0	A^1	$\mathbb{1} - I$
ε^1	0.03	ε^2	0.3

Initial values for the system variables, i.e. the phases and coupling strengths, were not parametrized explicitly, rather sampled from probability distributions. The initial phases $\varphi(0)_i^{1,2}$ are randomly and uniformly distributed around the unit circle for both layers, i.e. $\varphi(0)_i^{1,2} \sim \mathcal{U}[0, 2\pi]$. The intralayer coupling of the parenchymal layer coupling is also chosen randomly and uniformly distributed in the interval $[-1.0, 1.0]$. Since there is no self-coupling, the diagonal is set to 0.

For the immune layer an initial cytokine activation is modeled by clustering the initial intralayer coupling matrix. A smaller cluster of $C \cdot N$ oscillators and a bigger cluster of $(1 - C) \cdot N$ cells. Within the clusters oscillators are connected but not between the clusters. Following [43], the cluster size $C \in [0, 0.5]$ was chosen as 0.2, but as their findings suggest the size of the clusters does not have impact on the systems dynamics. An example for initial variable values of a system with $N = 200$ and $C = 0.2$ is shown in Figure 6.

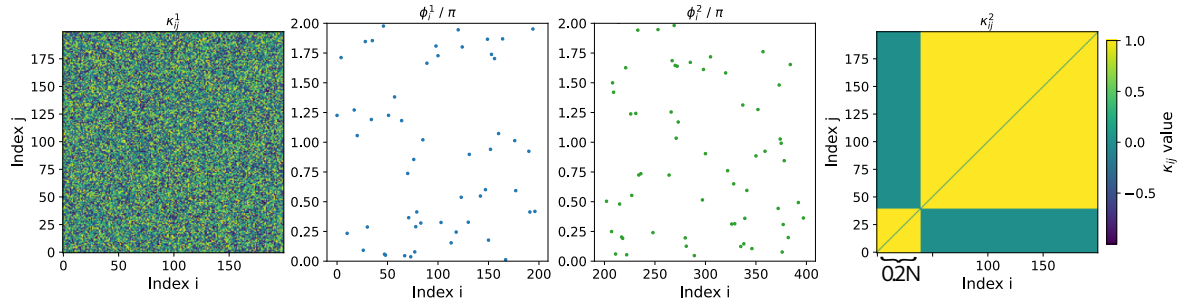


Figure 6: Initializations for the variable values of a DNM with $N = 200$ oscillators per layer. The middle two plots show the phases of the oscillators, with φ_i^1 for parenchymal and φ_i^2 for the immune layer, sampled from a uniform random distribution from 0 to 2π . On the left-hand side is the initialization of the parenchymal intralayer coupling matrix \mathbf{K}^1 from a uniform distribution in the interval from -1 to 1 . On the right-hand side is the two cluster initialization for the coupling matrix \mathbf{K}^2 of the immune layer, with a cluster size of $C = 0.2$, where each cluster is intra-connected, but without connections between the clusters.

To average out the influence of specific random initial values, simulations are performed for index ensembles, combining $m \in 1, \dots, M$ ensemble members. Throughout this work an ensemble size of $M = 50$ was used.

4.3.3. Synchronicity Metrics

As introduced in Section 4.1, for the complex Kuramoto networks the synchronization behavior is usually the point of interest, in the following two metrics are introduced, relevant to connect the DNM-dynamics to sepsis. There are two relevant states or system configurations that should be identifiable and quantifiable to allow qualified state analyzes: phase and frequency synchronization, for each a distinct measure is required.

Phase synchronization of a layer is commonly measured by the *Kuramoto Order Parameter* [49]:

$$R_2^{1,2}(t) = \frac{1}{N} \left| \sum_j^N e^{i \cdot \varphi_j^{1,2}(t)} \right| \quad \text{with } 0 \leq R_2^{1,2} \leq 1 \quad (4.7)$$

where $R_2^\mu = 0$ corresponds to total desynchronization, the splay-state and $R_2^\mu = 1$ corresponds to fully synchronized state, for convenience from now on the subscript \cdot_2 is omitted, denoting the Kuramoto Order Parameter simply as $R^{1,2}$.

Frequency synchronization measurements are more involved, as a starting point first the notion of a layers *mean phase velocity* has to be introduced, which can be calculated as follows:

$$\bar{\omega}^{1,2} = \frac{1}{N} \sum_j^N \dot{\varphi}_j^{1,2}(t) \quad (4.8)$$

The original definition uses an approximated version using the oscillators mean velocity:

$$\langle \widetilde{\dot{\varphi}_j^{1,2}(t)} \rangle = \frac{\varphi_j^{1,2}(t+T) - \varphi_j^{1,2}(t)}{T} \quad (4.9)$$

$$\widetilde{\bar{\omega}^{1,2}(t)} = \frac{1}{N} \sum_j^N \langle \widetilde{\dot{\varphi}_j^{1,2}(t)} \rangle \quad (4.9)$$

for some averaging time window T . But since their choice of T is not documented while having substantial influence on the calculation the instantaneous angle velocity from Equation (4.8) was preferred. Due to this change in definition, while the overall systematics stay the same, deviations from their original results are expected.

One can now calculate the *standard deviation of the mean phase velocities*:

$$\sigma_\chi(\bar{\omega}^{1,2}, t) = \sqrt{\frac{1}{N} \sum_j^N (\dot{\varphi}_j^{1,2}(t) - \bar{\omega}^{1,2}(t))^2} \quad (4.10)$$

Where $\sigma_\chi = 0$ indicates full frequency synchronization and growing values indicate desynchronization and/or clustering. Nonzero values only reveal that there is some desynchronization of the frequencies, but it remains unknown if it is clustered, multi-clustered or fully desynchronized.

Having multiple ensemble members $m = 1, \dots, M$ with the same parameterization, it is expected that different initialization, meaning initial-values drawn from the parameterized distributions, exhibit dissimilar behaviors, one can also calculate the *ensemble averaged standard deviation of the mean phase velocity*:

$$s^{1,2}(t) = \frac{1}{M} \sum_m^M \sigma_\chi(\bar{\omega}_m^{1,2}, t) \quad (4.11)$$

In [43] it was shown numerically that the quantity $s^{1,2}$ is proportional to the fraction of ensemble members that exhibit frequency clusters containing at least one oscillator. This makes s^1 a viable measure for pathology, as increasing values of s^1 or increasing system

incoherence then indicate more dysregulated host responses and consequently higher risks of multiple organ failure.

4.3.4. Simulation Results

The original findings of [43] identify β , the combined age parameter, and σ , the interlayer coupling strength which models the cytokine activity, as naturally important parameters in order to understand underlying mechanisms of sepsis progression. In the following subsection multiple simulation results are presented, starting with time-snapshots for different parameterization and initializations. Afterward, the transient and temporal behavior of the metrics $s^{1,2}$ and $R^{1,2}$ is for the same parameterization, as well as the introduction of the β, σ phase space of these metrics.

In Figure 7, snapshots of the system variables are shown for different parameterization, differing only in the choice β and σ , configurations A, B, C and D are listed in Table 3, other parameters are shared between the configurations and are stated in Table 2. Each configuration is expected to represent the current physiological state a single patient.

All following results are for a system with $N = 200$ oscillators, and snapshots taken at time $T_{\text{sim}} = 2000$, the end of the integration time, and show the stationary values at that time point.

Table 3: Specific β - σ combinations to illustrate simulation results.

	A	B	C	D
β	0.5π	0.58π	0.7π	0.5π
σ	1.0	1.0	1.0	0.2

In Figure 7, the left-most columns depicts the coupling matrices for the organ layer \mathbf{K}^1 followed by two columns showing the phase velocities for each oscillator $\dot{\varphi}_i^{1,2}$ and two columns showing the oscillator phases each layer $\varphi_i^{1,2}(T_{\text{sim}})$. The right-most column shows the coupling matrix for the immune layer \mathbf{K}^2 . Each layer is sorted first from lowest to highest frequency and secondary by lowest to highest phase for better clarity. Rows C and C' share the same parameterization but are different samples from the same initialization distributions.

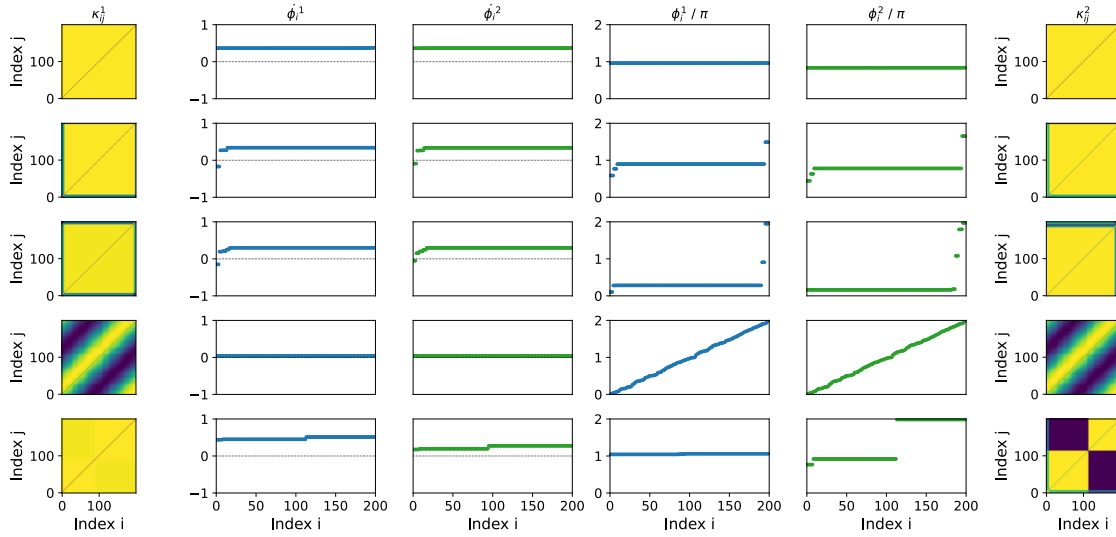


Figure 7: Snapshots of different DNM parametrization and initialization. Configuration A can be regarded as healthy, with phases and frequencies being fully synchronized. In contrast, B and C are pathologic, due to their clustering in $\dot{\phi}^1$. Configuration C' corresponds to a vulnerable state, because of uniformly distributed phases (splay state). Lastly, D is regarded as resilient, since the phases exhibit clustering, but the frequencies $\dot{\phi}^1$ are synchronized.

K colorbar

Row A in Figure 7 is fully synchronized/coherent since it not only has the frequencies synchronized but also the phases and can therefore interpreted as healthy. The coherence can also be seen in the fully homogeneous coupling matrices where both $\mathbf{K}^{1,2}$ show the same coupling strength for every oscillator pair. The rows B and C in contrast show signs of a pathological state, here both the frequencies three and phases have four distinct clusters respectively. The clusters are also visible in the coupling matrices, where the coupling strength differs based on the cluster.

The row for C', even though having the same parameterization as C, can be regarded vulnerable, since the phases uniformly distribute in the $[0, 2\pi]$ interval ($R^{1,2} = 0$), while the frequencies are synchronized. Coupling matrices for C' show traveling waves, which are characteristic for splay states. Observing different results for different initializations justifies the introduction of ensembles. Lastly row D shows a resilient state, where the phases are clustered while the frequencies are synchronized.

For the next result, the ensembles were introduced, every configuration of A, B, C, and D was simulated for $M = 50$ different initializations over an interval of $T_{\text{sim}} = 2000$. The two left-most columns show the standard deviation of the mean phase velocities $s^{1,2}$ for each ensemble member m . The plots show the temporal evolution of metrics for quantifying phase and frequency coherence, with the two right-most columns of Figure 8 show the temporal behavior of the Kuramoto Order Parameter for each individual ensemble member $m \in 1, 2, \dots, M$. Where lower values for $R^{1,2}$ indicate decoherence in phases, with its minimum $R^{1,2} = 0$ coincides with a splay state, and for $s^{1,2}$ higher values indicate a larger amount of frequency decoherence and clustering.

which is stronger?

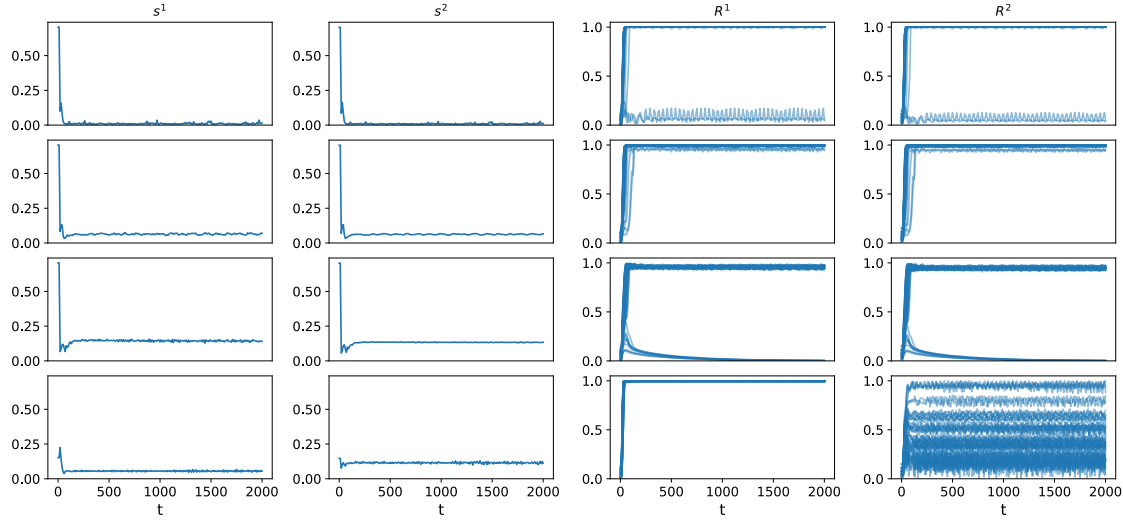


Figure 8: Transient and temporal evolution of the phase- and frequency-synchronization metrics $R^{1,2}$ and $s^{1,2}$, for ensembles of the DNM for the configurations listed in Table 3. Emphasizing the influence of β and σ on the systems synchronization behavior, and presenting different stable emergent system states.

Every ensemble in Figure 8 shows decoherence for early time-points, which is expected for randomly initialized variables, but changes relatively fast through a transient phase $t \in [0.0, 200]$ into systematic stable behavior. The stable states align with the observations made for Figure 7, configuration A has, besides small jitter, mostly synchronized frequencies $s^{1,2} \approx 0$. Also the phases of configuration A are mostly synchronized with $R^{1,2} \approx 1$, only two initializations show decoherence and are oscillating between weak clustering and almost full incoherence. Medically this can be interpreted as a low risk of a dysregulated host response for an otherwise healthy response to the initial cytokine activation. For configuration B the amount of incoherence inside the ensemble is clearly visible, with $s^{1,2}$ being positive and some more ensemble members exhibiting clustering, indicated by a Kuramoto Order Parameter slightly less than 1. In configuration C the incoherence is even more prominent, larger $s^{1,2}$ and some ensemble members evolving into a splay state, i.e. $R^{1,2} = 0$. For configuration D the overall phase incoherence is again a bit less compared to C, and lower for the organ compared to the immune layer. The phases are coherent for the organ layer but seem almost chaotic for the immune layer, some are synchronized, while others are clustered, in a chimera or almost splay-like state. Over the whole simulation period, the coherency in the immune layer seems not to fully stabilize, rather oscillate around an attractor.

Each of the configurations only differs in the parameter choices for β and σ , yet they evolve into unique and distinct system states. To put these four specific configurations into broader perspective, a grid of β and σ was simulated, in the interval $\beta \in [0, 1]$ with a grid resolution of 0.01 and $\sigma \in [0, 1.5]$ with a resolution of 0.015, creating a grid of 10,000 points. In Figure 9 the metric $s^{1,2}$ is shown in the $\beta - \sigma$ phase space for both layers in the first row, where brighter colors indicate a larger risk of frequency desynchronization, or risk of dysregulated immune response. The second row shows the ensemble mean over $\bar{R}^{1,2}$, i.e. $\bar{R}^{1,2} = \frac{1}{M} \sum_m^M R_m^{1,2}$, with $M = 50$, where darker colors indicate larger phase desynchronization. The white rectangle

indicates the simulated region in [43], $\beta \in [0.4, 0.7]$ and $\sigma \in [0, 1.5]$ for reference. Coordinates of the configurations A, B, C, and D are also labeled.

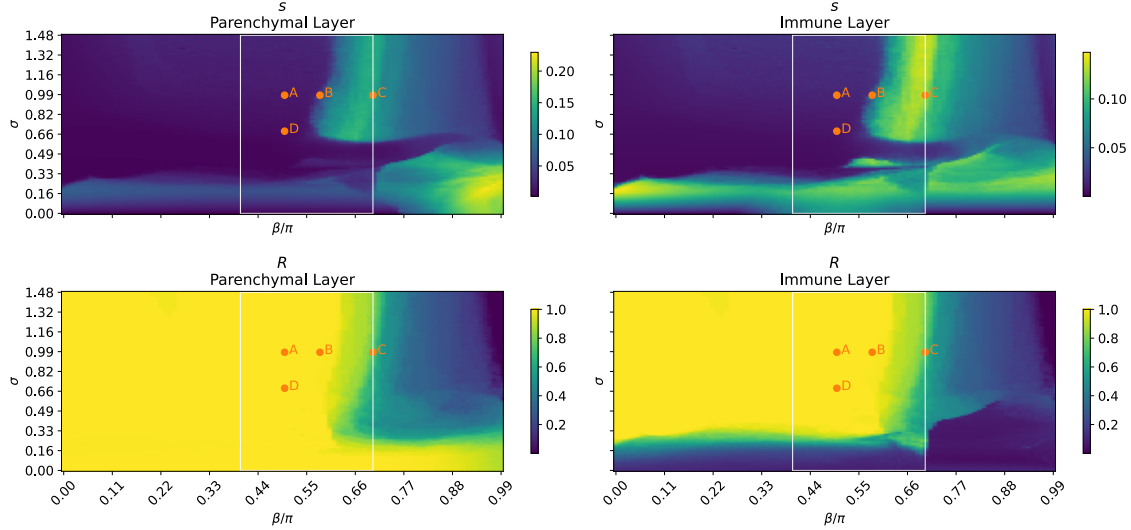


Figure 9: Phase space of the parameters β and σ and illustrating the broader picture their influence on the frequency and phase synchronization of the DNM. White rectangle indicates the grid-limits of the original publication [43].

Generally there is a similarity between phase and frequency desynchronization but no full equality, meaning there are parameter regions where the phase is synchronized and frequency desynchronized and vice versa. Another observation, that smaller values of $\beta < 0.55$ correspond to less desynchronization and stronger coherence, which is in line with the medical interpretation of β where smaller values indicate a younger and more healthy biological age. When crossing a critical value of $\beta_c \approx 0.55$ for the frequency and $\beta_c \approx 0.6$ for the phases, the synchronization behavior suddenly changes and tends towards incoherence, clustering and pathological interpretations.

For small values of $\sigma < 0.5$ the frequency synchronization and $\sigma < 0.25$ for the phase synchronization, the behavior significantly differs between immune and organ layer. The immune layer tends to fully desynchronize, instead the organ layer only the frequency desynchronizes for larger $\beta > 0.7$. With larger values of $\sigma > 0.5$ the dynamics more or less harmonize between layers and metrics and are mostly depend on β .

4.4. Limitations and Research Direction

While the DNM provides a structured, functional and biologically inspired model sepsis for dynamics, several limitations must be acknowledged when interpreting its physiological relevance.

Uniform and Symmetric Couplings: The fully connected intralayer topology (all oscillators inside a layer interact with each other), may not reflect actual cytokine networks behavior, where communication is spatially localized. Similarly the interlayer is modeled via uniform

connections which treats infected areas not different than healthy areas, even though the communication patterns are most likely not the same for both cases.

Selective Space Interpretation: In their original works, and adapted for this thesis, only a very small subspace has been simulated and interpreted [43]. For this selected subspace one can find regimes of synchronization, phase clustering and frequency clustering, which allow physiological interpretation. But what about the unexplored space, does it not align with existing medical knowledge?

Parameter Interpretability: Central parameters like β the medical age, σ the interlayer coupling, the phase lags α , and the timescale ratios ε do not correlate to any real observable quantity. This dimensionless formulation makes the model scale-free, which strengthens theoretical analysis but possibly weakens clinical translation.

Functional vs. Mechanistic: The DNM is explicitly functional, where individual oscillators do not correspond to specific cells, instead the model captures aggregated behavior. This abstraction brings the benefit of computational tractability, compared to mechanistic cell simulation, and simplified system state interpretation, but it also brings drawbacks of limited ability to identify which biological processes drive the observed dynamics. It boils down to the question: Does the functional description capture the essential dynamics of sepsis, or does it produce patterns that resemble physiological behavior without true correspondence?

These limitations reveal a gap: while the DNM demonstrates rich theoretical behavior that can be interpreted through a physiological lens, the model has not yet been validated against real patient data. To bridge this gap between theoretical considerations and clinical utility, this work investigates whether the DNM can be grounded in observable patient trajectories. Specifically, can the abstract parameters (β, σ) that govern the model behavior be inferred from real-world time-series data? And if so, does incorporating this physics-inspired structure provide advantages over purely data-driven approaches?

To summarize, the specific research questions include:

- **Usability of the DNM:** How and to what extent can the ML-determined trajectories of the DNM be used for detection and prediction, especially of critical infection states.
- **Comparison with data-based approaches:** How can the model-based predictions be compared with those of purely data-based approaches in terms of predictive power.

The first question directly addresses the parameter interpretability problem. If β and σ cannot be reliably inferred from clinical observations, or if inferred values lack predictive power for outcomes, the models clinical relevance remains speculative. Conversely, if DNM parameters learned from data correlate with disease severity and trajectory, this would suggest physiological correspondence to the model parameters.

The second question tackles the functional vs. mechanistic limitation. Does embedding the DNM structure as an inductive bias improve predictions compared to black-box models that ignore physiological principles? Or does the model's abstraction level sacrifice too much biological detail to be useful? This comparison will reveal whether the DNM's theoretical framework translates to practical advantages in clinical prediction tasks.

4.5. Summary of the DNM

This chapter introduced the Dynamic Network Model as a functional, mesoscopic description of coordinated physiological activity during sepsis, modeling cellular cytokine-based communication. Based on adaptive Kuramoto-type oscillators arranged in a two-layer parenchymal-immune architecture, the model exhibits a range of emergent regimes like synchronization, clustering, chimera-like patterns, that may be interpreted physiological states. Key parameters such as the biological age β and interlayer coupling σ were shown to modulate these regimes. However, the gap between theoretical considerations and clinical validation remains. The following chapters address this gap directly by developing methods to infer DNM parameters from real patient data and evaluating whether this physics-based structure provides predictive advantages over purely empirical approaches.

5 Method (Latent Dynamics Model)

This chapter introduces the methodological framework used to address the first research question as proposed in Section 4.4:

Usability of the DNM: How and to what extent can the ML-determined trajectories of the DNM be used for detection and prediction, especially of critical infection states and mortality.

As established in the previous chapter, the DNM provides a theoretical framework for understanding sepsis dynamics through coupled oscillator networks, but it has not yet been validated against real patient data. This chapter describes how the DNM can be embedded within a machine learning pipeline to enable parameter inference from clinical observations and probabilistic risk prediction.

Rather than predicting sepsis directly as a single binary outcome, proposed architecture decomposes the prediction task into two clinically meaningful quantities aligned with the Sepsis-3 definition. The Suspected Infection and increase in SOFA scores are predicted as proxies creating more nuanced and more interpretable prediction results.

The core idea is to embed the DNM into a learnable latent dynamical system. Here, a neural network learns to position patients into the (β, σ) -parameter phase space of the DNM and a recurrent neural network learns to predict the drift through that space based on observed clinical time series. The complete architecture, consisting of the DNM and additional auxiliary modules, will be referred to as the LDM from now on.

This chapter proceeds with Section 5.1, where the prediction task will be reiterated and the prediction strategy formalized. Desired prediction properties, together with the justification of modeling choices are also introduced here. Afterwards, in Section 5.2, the architecture will be discussed, focusing on what purpose each part serves and how it is integrated into the broader system.

5.1. Formalizing the Prediction Strategy

In automated clinical prediction systems, a patient is typically represented through their Electronic Health Record (EHR). The EHR aggregates multiple clinical variables, such as

laboratory biomarker, for example from blood or urine tests, or physiological scores and, further demographic information, like age and gender. Using the information that is available in the EHR until the prediction time-point t , the objective is to estimate the patients risk of developing sepsis at that time t . The following methodology will formalize the online-prediction, where newly arriving observations are continuously integrated into updated risk estimates. To use this prediction system in a clinical setting causality is important. Causality requires that for every prediction at time t only the information available up to that time-point can be used, and no future observations.

5.1.1. Patient Representation

Let t denote an observation time during a patients ICU-stay and the available EHR at that time consisting of D variables. After imputation of missing values, normalization, and encoding of non-numerical quantities, each variable μ_j is mapped to a numerical value:

$$\mu_{t,j} \in \mathbb{R}, \quad j = 1, \dots, D \quad (5.12)$$

These values are collected into a column-vector:

$$\boldsymbol{\mu}_t = (\mu_{t,1}, \dots, \mu_{t,D})^T \in \mathbb{R}^D \quad (5.13)$$

where the superscript $.^T$ denoting a transpose operation. The vector $\boldsymbol{\mu}_t$ is fully describing the current physiological state of the ICU-patient at observation time point t . It is used as the feature vector, meaning it does not carry information that directly translate to the sepsis definition.

5.1.2. Modeling the Sepsis-3 Target

The goal is derive continuously updated estimates of sepsis risk based on newly arriving observations $\boldsymbol{\mu}_t$ over time, with equally spaced and discrete time-steps $t \in \{0, \dots, T\}$. Following the Sepsis-3 definition, the onset of sepsis requires both suspected infection and acute multi-organ failure.

Defining the instantaneous *sepsis onset event* $S_t \in \{0, 1\}$ as the occurrence of the Sepsis-3 criteria at time point t within the patients ICU stay as:

$$S_t := A_t \wedge I_t \quad (5.14)$$

Here $A_t = \{\Delta O_t \geq 2\}$, indicates an acute worsening in organ function, measured via a change in SOFA-score $\Delta O_t = O_t - O_{\text{base}}$ with respect to some patient specific baseline SOFA-score O_{base} . The choice of O_{base} has to align with the Sepsis-3 definition, for example a 24 hours running minimum, the or $O_{\text{base}} = O_{t-1}$. The event I_t is an indicator for a Suspected Infection at time t defined according to the Sepsis-3 definition, spanning the 48 hours before and 24 hours after the documented SI-onset-time (see Section 2.2). Although the label I_t is defined retrospectively using a time window around the infection onset, this does not violate causality. The predictive model only conditions on $\boldsymbol{\mu}_{0:t}$, i.e., information available up to time

t . Future observations are used exclusively for label construction during training and are not available at inference time.

Conditioned on the history of observations $\mu_{0:t}$ the target probability is given by:

$$\Pr(S_t | \mu_{0:t}) = \Pr(A_t \cap I_t | \mu_{0:t}) \quad (5.15)$$

5.1.3. Heuristic Scoring and Risk Estimation

The direct estimation of the true conditional probability $\Pr(S_t | \mu_{0:t})$ is computationally and statistically challenging due to the temporal dependency between the binary Sepsis-3 criteria. To make the prediction of the target probability more tractable but still connect the statistical estimation to the clinical definition several assumptions and modeling choices are introduced.

Importantly, all assumptions result in differentiable approximations of the real events or probabilities, enabling end-to-end learning of estimators through gradient-based methods.

The central assumption is that infection I_t and multi-organ failure A_t are conditionally independent:

$$\Pr(A_t \cap I_t | \mu_{0:t}) = \Pr(I_t | \mu_{0:t}) \Pr(A_t | \mu_{0:t}) \quad (5.16)$$

Clinically this assumption does not hold, since the majority multi-organ failures stem from an underlying infection, meaning they exhibit strong partial correlations. Yet this assumption is necessary because the DNM, which is an essential building block to the LDM, only captures organ failure risk irrespective of infection states and the independence allows treating both components separately for the prediction. Additionally, this separation improves interpretability, since each component can be analyzed individually.

As a second assumption, although the indication I_t is binary, the prediction target is a temporally smoothed version. The surrogate label $\tilde{I}_t \in [0, 1]$ increases linearly in the 48 hours preceding the infection onset, it reaches maximum at onset, and it decays exponentially afterwards (24 hour window). This is mimicking temporal uncertainty of the diagnosis, for example due to delayed documentation and treatment effects such as antibiotic half-life.

Thus, the overall prediction requires two separate risk estimators:

$$\tilde{A}_t \approx \Pr(A_t | \mu_{0:t}) \quad \text{and} \quad \tilde{I}_t \approx \bar{I}_t \quad (5.17)$$

Both $\tilde{A}_t \in (0, 1)$ and $\tilde{I}_t \in (0, 1)$ are heuristic risk scores serving as approximations for the real event probabilities and the surrogate infection risk score. The original prediction target has been converted from a calibrated probability to a *heuristic risk score* \tilde{S}_t :

$$\Pr(S_t | \mu_{0:t}) \approx \tilde{S}_t := \tilde{A}_t \tilde{I}_t \quad (5.18)$$

The interaction term $\tilde{A}_t \tilde{I}_t$ mirrors their logical conjunction in the Sepsis-3 definition. It is important to note that \tilde{S} is **not a calibrated probability** but a heuristically derived and empirical risk score based on the Sepsis-3 definition, serving as a differentiable surrogate for the Sepsis-3 sepsis onset criterion $P(S_t | \mu_{0:t})$. Larger values of \tilde{S}_t correspond to higher expected risk of sepsis outbreak.

5.1.4. From EHR to Risk Scores

The high-dimensional EHR history $\mu_{0:t}$ must now be condensed into these two clinically motivated statistics \tilde{A}_t and \tilde{I}_t . The LDM architecture implements two learned mappings:

Infection risk estimation: A data-driven module directly estimates infection risk from the EHR history:

$$\tilde{I}_t = f(\mu_{0:t}; \theta_f) \quad (5.19)$$

where $f(\cdot; \theta_f)$ represents a neural network with learnable parameters θ_f that will be specified in Section 5.2.

Organ dysfunction estimation: Rather than directly predicting \tilde{A}_t from the EHR, the LDM uses an intermediate representation, a latent SOFA-score estimate:

$$\hat{O}_t := g(\mu_{0:t}; \theta_g) \quad (5.20)$$

where \hat{O}_t denotes a latent, differentiable estimation for the true SOFA-score O_t . The function $g(\cdot; \theta_g)$ represents a combined DNM pipeline, where θ_g combines all learnable parameters of that pipeline. Again the function is further specified in Section 5.2.

Given two consecutive estimated SOFA-scores \hat{O}_{t-1} and \hat{O}_t a differentiable increase indicator \tilde{A}_t is calculated to indicate the event of organ failure:

$$\tilde{A}_t = o_{s,d}(\hat{O}_{t-1:t}) = \text{sigmoid}(s(\hat{O}_t - \hat{O}_{t-1} - d)) \quad (5.21)$$

The function $o_{s,d}(\cdot)$ contains two globally learnable parameters, d a threshold and s a sharpness parameter. While the Sepsis-3 definition corresponds to a fixed threshold of $d = 2$, here d is treated as learnable to obtain a smooth, fully differentiable approximation of the discrete SOFA increase criterion and to account for uncertainty in baseline estimation. The choice of the function

$$\text{sigmoid}(x) = \frac{1}{1 + e^{-x}} \quad (5.22)$$

yields a monotonic indicator (larger SOFA increase \rightarrow more likely organ failure) while still being differentiable.

5.2. Architecture

The previous subsection explained how the sepsis onset target even S_t can be decomposed into the conjunction of suspected infection indication I_t and organ failure event A_t that itself can be calculated from two consecutive SOFA-scores $O_{t-1:t}$. The presented Latent Dynamics Model is designed to estimate the fundamental components \tilde{O}_t and \tilde{I}_t from a history of EHR $\mu_{0:t}$ to derive the heuristic sepsis risk score $\tilde{S}_t \approx S_t$ for individual patients. Each component is estimated by Recurrent Neural Networks (RNN) module, e.g. GRU or LSTM, enabling continuous estimation updates based on newly arriving measurements.

The following subsection will introduce the individual modules which are fully differentiable functions with learnable parameters allowing for optimization via first order gradient descent methods. Starting with the estimator module for the suspected infection indication module in Section 5.2.1, followed the organ failure estimation module in Section 5.2.2 which includes the DNM to derive SOFA estimates and lastly an auxiliary regularization module in Section 5.2.3.

Table 4: Summarization of notation used in the Latent Dynamics Model methodology.

SYMBOL	DESCRIPTION
i, N	Patient index and total patients
t, T_i	Time point and trajectory length
$\mu_t \in \mathbb{R}^D$	EHR vector with D variables at time t
$\mu_{0:t}$	EHR history from time 0 to t
$S_t, A_t, I_t \in \{0, 1\}$	Binary sepsis onset, organ failure, and infection events
$O_t, \Delta O_t \in [0, \dots 24]$	SOFA score and change from baseline
$\bar{I}_t \in [0, 1]$	Continuous surrogate infection indicator
$\hat{O}_t \in \{0, \dots 24\}$	Estimated SOFA score
$o_{s,d}(\hat{O}_{t-1:t})$	Differentiable increase detection function
$\tilde{S}_t, \tilde{A}_t, \tilde{I}_t \in (0, 1)$	Predicted sepsis, organ failure, and infection risks
$z = (z_\beta, z_\sigma)$	Latent coordinates in DNM parameter space
$\hat{z}_t, \Delta \hat{z}_t$	Predicted latent position and change
$s^1(z)$	Synchronization measure (desynchronicity) in DNM
$h_t \in \mathbb{R}^h$	Hidden state vector
$f_\theta, g_\theta^e, g_\theta^r, d_\theta$	Infection indicator, encoder, recurrent, decoder modules
θ	Learnable parameters
$\mathcal{L}_{\text{sepsis}}, \mathcal{L}_{\text{inf}}, \mathcal{L}_{\text{sofa}}$	Primary sepsis, infection, and SOFA losses
$\mathcal{L}_{\text{focal}}, \mathcal{L}_{\text{diff}}, \mathcal{L}_{\text{dec}}, \mathcal{L}_{\text{spread}}$	Auxiliary focal, directional, decoder, and diversity losses
λ_i	Loss weight for component i
B	Mini-batch size

5.2.1. Infection Indicator Module

The first module of the LDM estimates the presence of a SI, represented by the continuous surrogate indicator \bar{I}_t , the module predicts a continuous surrogate infection risk $\tilde{I}_t \in (0, 1)$. Given N patient trajectories with T_i pairs of EHR vectors and ground truth SI-indicator each:

$$(\mu_{i,t}, \bar{I}_{i,t}), \quad i = 1\dots N, \quad t = 1\dots T_i \quad (5.23)$$

a parameterized nonlinear recurrent function

$$f_{\theta_f} : \mathbb{R}^D \times \mathbb{R}^{H_f} \rightarrow (0, 1) \times \mathbb{R}^{H_f} \quad (5.24)$$

is trained to map the patients physiological state represented by the EHR to an estimated risk of suspected infection:

$$(\tilde{I}_t, \mathbf{h}_t) = f_{\theta_f}(\boldsymbol{\mu}_t, \mathbf{h}_{t-1}) \quad (5.25)$$

The hidden state h_t propagates temporal information through time. For the first time-step $t = 0$ a learned initial hidden state h_0 is used.

The model is implemented as a RNN, illustrated in Figure 10. At each timestep, a recurrent cell updates the hidden state, and a learned linear projection followed by sigmoid activation produces the infection risk estimate:

$$h_t = \text{RNN-Cell}_{\theta_f^{\text{rnn}}}(\mu_t, h_{t-1}) \quad (5.26)$$

$$\tilde{I}_t = \text{sigmoid}(\mathbf{w}_f \mathbf{h}_t + b_f) \quad (5.26)$$

where $\theta_f = \{\theta_f^{\text{rnn}}, \mathbf{w}_f, b_f\}$ combines all learnable parameters.

To fit the model, given a mini-batch of size B , Binary Cross Entropy (BCE) loss which measures the distance between true label \bar{I}_t and the predicted label \tilde{I}_t :

$$\mathcal{L}_{\text{inf}} = -\frac{1}{B} \sum_{i=1}^B \frac{1}{T_i} \sum_{t=1}^{T_i} \left[\bar{I}_{i,t} \log(\tilde{I}_{i,t}) + (1 - \bar{I}_{i,t}) \log(1 - \tilde{I}_{i,t}) \right] \quad (5.27)$$

is minimized and thus the estimator provides a differentiable estimate of the surrogate infection activity.

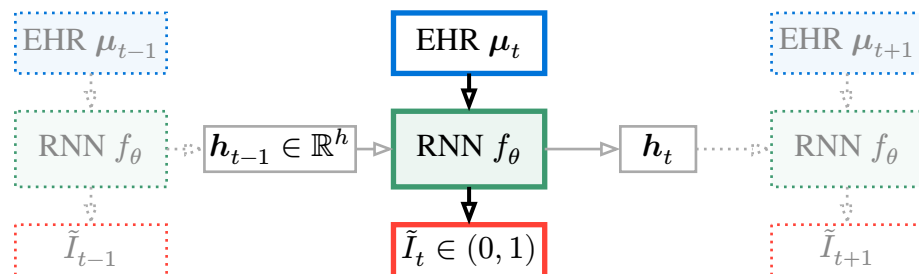


Figure 10: Schematic of the Infection Indicator Module architecture and rollout. The RNN processes the EHR sequence $\mu_{0:T}$ step-by-step, maintaining h_t to capture temporal dependencies, and outputs infection risk estimates \tilde{I}_t at each timestep.

5.2.2. SOFA Predictor Module

The complete SOFA predictor module g_θ is composed two submodules, an initial-encoder g_θ^e and a recurrent latent predictor g_θ^r , each described below. The idea is to translate the physiological patient trajectory to a sequence of the DNM parameters β and σ , where the desynchronization of given parameter pairs should match the physiological organ failure. To begin with, Section 5.2.2.1 once more tries to strengthen the connection between organ failure and the DNM, followed by Section 5.2.2.2 presents how the EHR information is embedded evolved inside the DNM parameter space. Lastly Section 5.2.2.3 describes how computational cost can be significantly reduced by precomputing the DNM parameter space.

5.2.2.1. The DNM as SOFA Surrogate

Recalling that the pathological organ conditions within the DNM are characterized by frequency clustering in the parenchymal layer. The amount of frequency clustering is quantified by the ensemble average standard deviation of the mean phase velocity s^1 (see Equation (4.11)). Since s^1 monotonically increases with loss of frequency synchronization, it serves as an interpretable and natural surrogate for the SOFA-score. Increasing values of s^1 indicate a higher SOFA-score and a worse condition of the patients organ system.

Numerical integration of the DNM equations for a given parameter pair $z = (\beta, \sigma)$ yields the corresponding continuous SOFA approximation $\hat{O}(z)$:

$$\hat{O}(z) = \left\lfloor \frac{24 \cdot s^1(z)}{s_{\max}^1} \right\rfloor = \left\lfloor \frac{24 \cdot s^1(\beta, \sigma)}{s_{\max}^1} \right\rfloor \quad (5.28)$$

these two parameters were identified as highly influential and interpretable quantities in the original DNM publications [43]. Every other system parameter is assumed constant and chosen as listed in Table 2. The rounding operation is used only for interpretability and evaluation; during training the normalized continuous s^1 -based surrogate is used.

The space spanned by the two parameters is called the *latent space*, coordinate-pairs of that latent space are denoted $z = (z_\beta, z_\sigma)$. In the following $s^1(z)$ and $\hat{O}(z)$ are used synonymously, depending on the context the notation emphasizes the connection to either the DNM or the interpretation as SOFA-score.

The prediction strategy involves the mapping of individual EHR to the latent space, so that the ground truth SOFA aligns with the desynchronization measure of the latent coordinate. Based off of this initial location (and additional information), the patient will perform a trajectory through the latent space yielding step by step SOFA-score $\hat{O}_{0:T}(z)$ estimates needed to calculate the heuristic organ-condition statistic \tilde{A}_t .

5.2.2.2. Latent Parameter Dynamics

Focusing on a single patient, but omitting the i subscript for readability, with its first observation at time $t = 1$, an encoder connects the high-dimensional EHR to the dynamical regime of the DNM, a neural encoder:

$$g_{\theta_g^e}^e : \mathbb{R}^D \rightarrow \mathbb{R}^2 \times \mathbb{R}^{H_g} = \mathbb{R}^{2+H_g} \quad (5.29)$$

where the high dimensional patient state is mapped to a two-dimensional latent vector, and a H_g -dimensional hidden state.

$$(\hat{z}_0^{\text{raw}}, \mathbf{h}_0) = \left((\hat{z}_{0,\beta}^{\text{raw}}, \hat{z}_{0,\sigma}^{\text{raw}}), \mathbf{h}_0 \right) = g_{\theta_g^e}^e(\boldsymbol{\mu}_0) \quad (5.30)$$

This encoding locates the patient within a physiologically meaningful region of the DNM parameter space, which in context of the LDM is called the latent space. To keep all of the latent coordinates in a reasonable predefined area they are ultimately transformed by:

$$\hat{z} = \text{sigmoid}(\hat{z}^{\text{raw}}) \cdot \left(\frac{\beta_{\max} - \beta_{\min}}{\sigma_{\max} - \sigma_{\min}} \right)^T + \left(\frac{\beta_{\min}}{\sigma_{\min}} \right)^T \quad (5.31)$$

The latent coordinate \hat{z}_0 provides the initial condition for short-term dynamical organ condition forecasting. As described in Section 5.2.2.1 the latent coordinates correspond to a DNM synchronization behavior and can therefore be directly interpreted as SOFA-score estimates ($\hat{z} \rightarrow s^1(\hat{z}) \rightarrow \hat{O}(\hat{z})$).

In addition to the estimated parameter pair \hat{z}_0^{raw} , the encoder outputs another vector with dimension $H_g \ll D$ that is a compressed representation of patient physiology relevant for short-term evolution of \hat{z} . This vector $\mathbf{h}_0 \in \mathbb{R}^{H_g}$ is the initial hidden space.

Since the heuristic SOFA risk \tilde{A} depends on the evolution of organ function $\hat{O}_{0:t}$, it is necessary to estimate not only the initial state \hat{z}_0 but also its evolution. For this purpose a neural recurrent function:

$$g_{\theta}^r : \mathbb{R}^{D+2} \times \mathbb{R}^{H_g} \rightarrow \mathbb{R}^2 \times \mathbb{R}^{H_g} \quad (5.32)$$

is trained to propagate the latent DNM parameters forward in time.

This recurrent mechanism, conditioned on the hidden state \mathbf{h}_t and previous latent location $\hat{z}_{t-1}^{\text{raw}}$, captures how the underlying physiology influences the drift of the DNM parameters. From the previous hidden state and latent-position a recurrent cells updates the hidden state, followed by a linear down-projection to receive the updated latent-position.

$$\mathbf{h}_t = \text{RNN-Cell}_{\theta_g^{\text{rnn}}}((\boldsymbol{\mu}_t, \hat{z}_{t-1}^{\text{raw}}), \mathbf{h}_{t-1}), \quad t = 2, \dots, T \quad (5.33)$$

$$\Delta \hat{z}_t^{\text{raw}} = (\mathbf{w}_g \mathbf{h}_t) \quad (5.33)$$

$$\hat{z}_t^{\text{raw}} = \hat{z}_{t-1}^{\text{raw}} + \Delta \hat{z}_t^{\text{raw}} \quad (5.33)$$

where $\theta_g^r = \{\theta_g^{\text{rnn}}, \mathbf{w}_g\}$ combines all of the learnable parameters.

Depending on the movement in the latent space the level of synchrony changes across the prediction horizon, which translates to the pathological evolution of patients. The online-prediction rollout is shown in figure Figure 11.

By predicting the movement in the latent space $\Delta\hat{z}_t$ instead of the raw parameters, smooth trajectories can be learned. For the latent sequence this is more desirable compared to the infection indicator, where jumps in predicted values do not matter as much.

To fit the functions, here the placement of latent points \hat{z} is guided by a supervision signal:

$$\mathcal{L}_{\text{sofa}} = \frac{1}{B} \sum_{i=1}^B \frac{1}{T_i} \sum_{t=1}^{T_i} w_{O_{i,t}} \cdot \left(\frac{O_{i,t}}{24} - \frac{s_{i,t}^1(\hat{z})}{s_{\max}^1} \right)^2 \quad (5.34)$$

where the class-balancing weight:

$$w_O = \log(1 + f_O^{-1}) \quad (5.35)$$

with f_O being the relative frequency of SOFA-scores O . This inverse-frequency weighting up-weights rare high SOFA-scores that are clinically critical but statistically underrepresented. Also notice that both parts, i.e. the continuous approximation (given by the desynchronicity) and ground truth are scaled to the interval $[0, 1]$.

Because gradients can flow backwards through the whole sequence, minimizing the loss can jointly train the encoder g_θ^e and recurrent function g_θ^r .

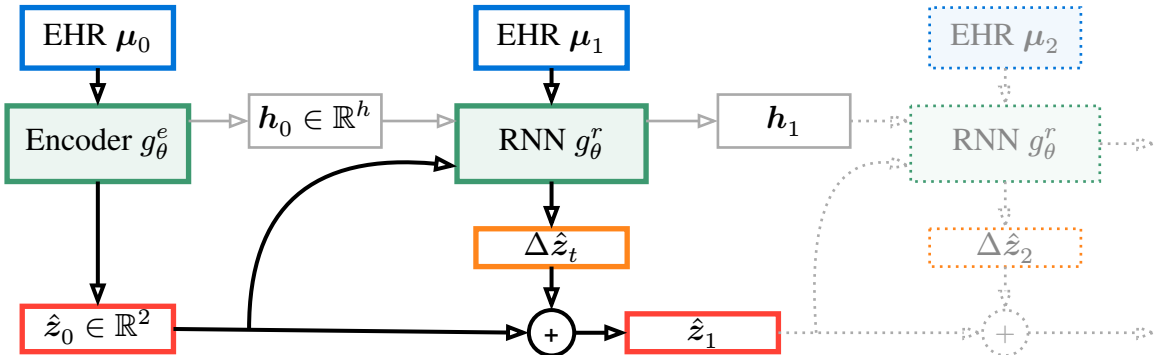


Figure 11: Architecture and online-prediction rollout of the SOFA Predictor Module.

Raws

5.2.2.3. Latent Lookup

Intuitively one would numerically integrate the DNM every estimate \hat{z} to receive the $s_{\hat{z}}^1$ -metric for the continuous space in (β, σ) . But to massively reduce the computational burden the space has been quantized to a discrete and regular grid, with the metric pre-computed for each coordinate pair. The space is limited to the intervals $\beta \in [0.4\pi, 0.7\pi]$ and $\sigma \in [0.0, 1.5]$ (the phase space of the original publication [43]). Instead of integrating the DNM over and over, differentiable approximation values are retrieved from the precomputed grid by using localized soft interpolation.

For an estimated coordinate pair $\hat{z} = (\hat{z}_\beta, \hat{z}_\sigma)$ in the continuous (β, σ) -space the quantized metrics are interpolated by smoothing nearby quantization points with a Gaussian-like kernel, which is illustrated in Figure 12.

To enable gradient-based optimization, the lookup of nearby points \tilde{z}' combines two mechanisms: (1) a straight-through estimator [55] for the discrete voxel indexing operation, allowing gradients to flow as if the rounding were identity, and (2) differentiable softmax interpolation over neighboring grid points. This hybrid approach allows for efficient nearest-neighbor lookup in the forward pass while providing meaningful gradients for the continuous query coordinates \hat{z} .

The nearby points are selected by a quadratic slice around the closest quantized point \tilde{z} , with k being the sub-grid size:

$$\tilde{z} = \hat{z} + \text{stop_grad}(\lfloor \hat{z} \rfloor - \hat{z}) \quad (5.36)$$

$$\tilde{s}^1(\hat{z}) = \sum_{z' \in \mathcal{N}_{k \times k}(\tilde{z})} \text{softmax}\left(-\frac{\|\hat{z} - z'\|^2}{T_d}\right) s^1(z') \quad (5.36)$$

with softmax for $K = k \cdot k$ neighboring points being:

$$\text{softmax}(x)_j = \frac{e^{x_j}}{\sum_{k=1}^K e^{x_k}}, \quad \text{for } j = 1, \dots, K \quad (5.37)$$

and:

$$\mathcal{N}_{k \times k}(\tilde{z}) = \{(\tilde{z}_\beta + i \cdot \beta_{\text{step size}}, (\tilde{z}_\sigma + j \cdot \sigma_{\text{step size}})) \mid i, j \in \{-1, 0, 1\}\} \quad (5.38)$$

With $T_d \in \mathbb{R}_{>0}$ being a learnable temperature parameter which controls the sharpness of the smoothing, with larger values producing stronger smoothing and smaller values converging to the value of the closest point \tilde{z} exclusively.

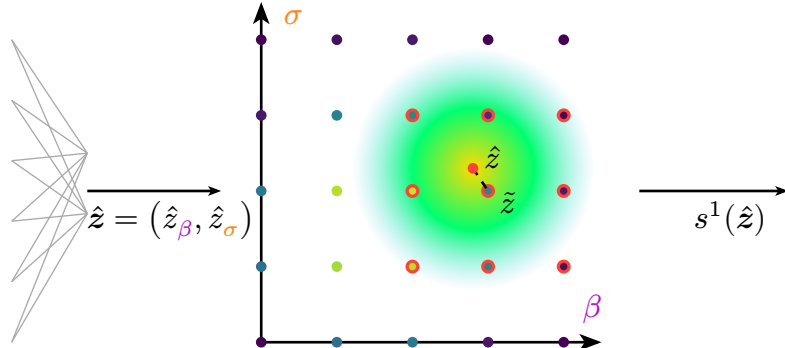


Figure 12: Quantized latent lookup of precomputed synchronization metrics. Point colors represent the amount of desynchronization s^1 in the parenchymal layer. Neighboring points, the $z' \in \mathcal{N}_{3 \times 3}(\tilde{z})$ sub-grid indicated by the red outlines around \tilde{z} , are used smoothed using a Gaussian-like kernel, represented by the color gradient around estimation point \hat{z} . This allows continuous interpolation the parameter space.

This quantization strategy allows for continuous space approximation from the quantized space, while also making it possible to pre-compute the quantized space and therefore drastically reducing the computational expenses. This quantization strategy, called *latent lookup*² is closely related to Finite Scalar Quantization (FSQ) [56], used in Dreamer-V3 [57] for

²Implementation is available at https://github.com/unartig/sepsis_osc/blob/main/src/sepsis_osc/lsm/lookup.py

example. Unlike in this approach the values of the latent coordinates in Dreamer-V3 do not have prior semantic meaning associated with them. Both allow for differentiable quantization, with details on the latent lookup implementation, including grid-resolution and kernel size, can be found in Section 6.2.

In Neural Differential Equations [58] and Physics Informed Neural Networks [59] where the integration of the ODE itself provides gradients directly by backpropagation through the ODE. In contrast, here the gradient information is provided by the nearby quantized points which contribute to estimated synchronicity measure through the smoothing.

5.2.3. Decoder

As shown in the visualization of the DNM phase space in Figure 9 multiple latent coordinates \mathbf{z} result in the same amount of desynchronization, which is not surprising, since different physiological states share the same SOFA level. But when different physiological states have a common SOFA-score but from different physiological reasons, their latent representations should be different and unique to that exact physiological state. This should enable to distinguish different triggers of the organ failure inside the latent space, similarly to how it is possible to distinguish the different triggers from the EHR.

In a classical Auto-Encoder [60] setting, to encourage a semantically structured latent space, a decoder module is added as an auxiliary regularization component. A neural decoder network:

$$d_\theta : \mathbb{R}^2 \rightarrow \mathbb{R}^n \quad (5.39)$$

attempts to reconstruct the original EHR features from the latent representation, the resulting desynchronicity of that latent coordinate and the heuristic risk measures:

$$\hat{\boldsymbol{\mu}}_t = d_\theta(\hat{\mathbf{z}}_t) \quad (5.40)$$

This way the decoder only learns to disentangle the latent coordinates in $\hat{\mathbf{z}}_t$ based on ground future EHRs $\boldsymbol{\mu}_t$, through a supervised loss:

$$\mathcal{L}_{\text{dec}} = \frac{1}{B} \sum_{i=1}^B \frac{1}{T_i} \sum_{t=0}^{T_i-1} (\boldsymbol{\mu}_{i,t} - \hat{\boldsymbol{\mu}}_{i,t})^2 \quad (5.41)$$

This latent regularization is motivated by *Representation Learning* [60] and ensures that nearby points in the latent (β, σ) -space correspond to physiologically similar patient states. It helps the encoder g_θ^e to learn a meaningful alignment between EHR-derived latent-embeddings and the dynamical DNM landscape.

Using this regularization the latent encoder g_θ^e and the recurrent predictor g_θ^r are encouraged to map temporally consecutive to spatially near latent coordinates, since it is expected that consecutive EHRs do not exhibit drastic changes. Leading smooth patient trajectories through the latent space.



Figure 13: Data flow of the decoder module.

5.2.4. Training Objective and Auxiliary Losses

The complete LDM is trained end-to-end by combining the previously introduced Infection Indicator Module f_θ and the SOFA prediction module g_θ . The output of these modules yield the components \hat{O}_t , from which \tilde{A}_t can be derived (Equation (5.21)) and \tilde{I}_t , taking these components one can calculate the heuristic sepsis onset risk $\tilde{S}_t = \tilde{A}_t \tilde{I}_t$.

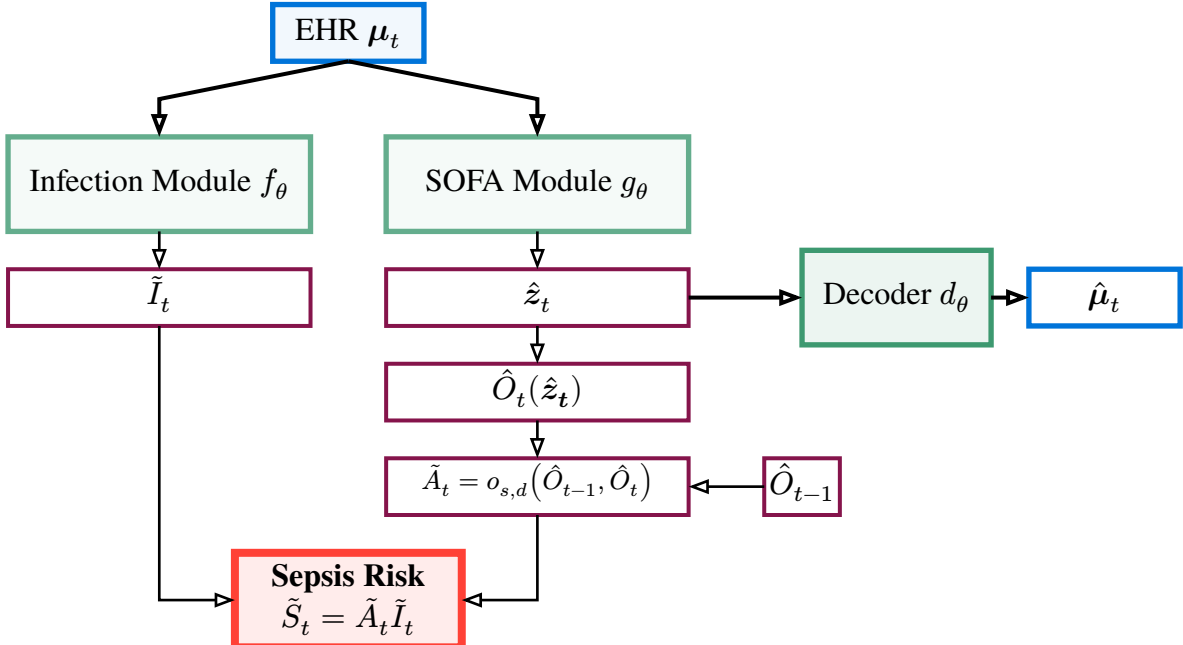


Figure 14: Schematic of a single prediction step of the LDM, with the direct \tilde{I}_t prediction and the multiple steps to derive \tilde{A}_t . If no \hat{O}_{t-1} is available at the first time-step, the heuristic organ failure risk is assumed to be 0.

Besides the losses already presented, to guide the training process multiple auxiliary losses are used and introduced in the following.

Primary Sepsis Prediction Loss

The main training signal aligns the heuristic sepsis score \tilde{S}_t with ground truth sepsis labels:

$$\mathcal{L}_{\text{sepsis}} = -\frac{1}{B} \sum_{i=1}^B \frac{1}{T_i} \sum_{t=0}^{T_i-1} [S_{i,t} \log(\tilde{S}_{i,t}) + (1 - S_{i,t}) \log(1 - \tilde{S}_{i,t})] \quad (5.42)$$

again using the BCE. Because positive labels may be temporally windowed around the true onset of sepsis, the estimated sepsis risk score is computed via causal smoothing:

$$\tilde{S}_t = \text{CS}(\tilde{A}_t) \cdot \tilde{I}_t \quad (5.43)$$

where $\text{CS}(\cdot)$ denotes a causal smoothing operator that maintains elevated predictions in the time-steps preceding sepsis onset. The causal smoothing operation is defined as:

$$\text{CS}(x_t) = \sum_{\tau=0}^r w_\tau \cdot x_{t-\tau}, \quad w_\tau = \frac{e^{-\alpha\tau}}{\sum_{k=0}^r e^{-\alpha k}} \quad (5.44)$$

with radius r is a hyper-parameter controlling the temporal radius of the smoothing window, and α a learnable decay parameter controlling the length and shape of the smoothing kernel. To handle the sequence boundaries $x_{t-\tau} = 0$ for $t - \tau < 0$.

This smoothing ensures that organ failure predictions remain elevated during the causal window preceding sepsis onset, matching the clinical reality that organ dysfunction typically precedes documented sepsis.

Organ Failure Alignment

To improve the sharpness of organ failure detection, a focal loss [61] penalizes misclassification of the discrete organ failure event:

$$\mathcal{L}_{\text{focal}} = -\frac{1}{B} \sum_{i=1}^B \sum_{t=0}^{T_i-1} \alpha (1 - p_{i,t})^\gamma \log(p_{i,t}) \quad (5.45)$$

with $p_{i,t} = A_{i,t} \cdot \tilde{A}_{i,t} + (1 - A_{i,t} \cdot (1 - \tilde{A}_{i,t}))$, the hyper-parameter γ controlling focus on hard examples and α emphasizing positive vs. negative samples. The well established focal loss has been proven to improve performance for high imbalance datasets, which is the case for rare events such as the SOFA increase. With this loss the model is encouraged to align the timing of predicted SOFA increase with the ground truth.

Difference Alignment

To encourage temporally coherent latent dynamics that align with ground truth SOFA progression:

$$\mathcal{L}_{\text{diff}} = \frac{1}{B} \sum_{i=1}^B \sum_{t=0}^{T_i-1} \sum_{t'=t+1}^{T_i-1} w_{t,t'} \cdot \text{ReLU}(-a_{t,t'}) \quad (5.46)$$

where the alignment term measures directional consistency between predicted and true SOFA changes:

$$a_{t,t'} = (\hat{O}_{t'} - \hat{O}_t) \cdot (O_{t'} - O_t) \quad (5.47)$$

and the weight emphasizes larger ground truth changes:

$$w_{t,t'} = |O_{t'} - O_t| + 1 \quad (5.48)$$

The Rectified Linear Unit (ReLU) activation penalizes only misaligned directions (when $a_{t,t'} < 0$), meaning the predicted change points in the opposite direction to the true change. This loss ensures that if a patient's true SOFA-score increases between time t and t' , the predicted score also increases (and vice versa for decreases), without strictly enforcing the magnitude of change.

Latent Space Regularization

To prevent collapse and ensure diverse latent representations:

$$\mathcal{L}_{\text{spread}} = -\log(\text{trace}(\text{Cov}(\hat{\mathbf{Z}}))) \quad (5.49)$$

where $\hat{\mathbf{Z}}$ collects all predicted latent coordinates in a batch and $\text{Cov}(\cdot)$ computes the sample covariance matrix.

The loss is minimized when the total variance of the latent dimensions β and σ increases and it therefore encourages a larger spread inside the latent space.

Boundary Loss

5.2.5. Combined Objective

The complete LDM³ is trained end-to-end by jointly optimizing all components with the weighted total loss:

$$\mathcal{L}_{\text{total}} = \lambda_{\text{inf}} \mathcal{L}_{\text{inf}} + \lambda_{\text{sofa}} \mathcal{L}_{\text{sofa}} + \lambda_{\text{dec}} \mathcal{L}_{\text{dec}} + \lambda_{\text{sepsis}} \mathcal{L}_{\text{sepsis}} + \quad (5.50)$$

$$\lambda_{\text{diff}} \mathcal{L}_{\text{diff}} + \lambda_{\text{focal}} \mathcal{L}_{\text{focal}} + \lambda_{\text{spread}} \mathcal{L}_{\text{spread}} \quad (5.50)$$

The loss weights λ_i balance the contribution of each objective during training. The primary sepsis prediction loss $\mathcal{L}_{\text{sepsis}}$ provides the main learning signal aligned with the clinical task, while component losses \mathcal{L}_{inf} and $\mathcal{L}_{\text{sofa}}$ ensure accurate estimation of the underlying infection and organ failure indicators. The auxiliary losses ($\mathcal{L}_{\text{focal}}$, $\mathcal{L}_{\text{diff}}$, \mathcal{L}_{dec} , $\mathcal{L}_{\text{spread}}$) regularize the latent space structure and temporal dynamics to improve generalization and interpretability.

All modules f_θ , g_θ^e , g_θ^r , and d_θ are jointly optimized through backpropagation, with gradients flowing through the differentiable DNM lookup mechanism described in Section 5.2.2.3. Specific values for the loss weights λ_i and other hyper-parameters are reported in Section 6.2.

Table 5 provides an overview of all loss components, their purpose, and the modules they supervise.

Table 5: Overview of loss components in the LDM training objective.

LOSS	TYPE	PURPOSE	SUPERVISES
$\mathcal{L}_{\text{sepsis}}$	BCE	Primary sepsis prediction	$f_\theta, g_\theta^e, g_\theta^r$
\mathcal{L}_{inf}	BCE	Infection indicator	f_θ
$\mathcal{L}_{\text{sofa}}$	Weighted MSE	SOFA estimation	g_θ^e, g_θ^r
$\mathcal{L}_{\text{focal}}$	Focal	Organ failure timing	g_θ^e, g_θ^r
$\mathcal{L}_{\text{diff}}$	Directional	Difference timing	g_θ^r
\mathcal{L}_{dec}	MSE	Latent semantics	$d_\theta, (g_\theta^e, g_\theta^r)$
$\mathcal{L}_{\text{spread}}$	Covariance	Latent diversity	g_θ^e, g_θ^r

³Implementation of the LDM components is available at https://github.com/unartig/sepsis_osc/tree/main/src/sepsis_osc/lmd

5.3. Summary of Methods

This chapter introduced the proposed model for short-term and interpretable risk prediction of developing sepsis for ICU patients, referred to as Latent Dynamics Model. Starting from the formal task definition, the full processing pipeline and detailed the architecture of the encoder, recurrent latent dynamics module, decoder, and the infection-indicator classifier have been presented. A key component of the approach is the integration of the functional DNM into the latent dynamics, enabling physiologically meaningful and interpretable temporal modeling.

The training losses used for each component and additional auxiliary losses were defined and how they contribute to the overall optimization objective. Finally the chapter also introduced the notation and training setup that will be used throughout the remainder of the thesis.

The next Section 6 presents the Medical Information Mart for Intensive Care (MIMIC)-IV database, a widely used ICU used to benchmark sepsis prediction models, and the exact task and cohort definitions used for baseline comparisons. The relevant evaluation metrics Area Under Receiver Operationg Curve (AUROC) and Area Under Precision Recall Curve (AUPRC) used to assess the predictive performance are introduced.

The chapter concludes with implementation details for training the LDM on the MIMIC-IV data and specific architectural choices. Final quantitative and qualitative results are presented and analyzed in Section 7.

INFERENCE

6 Experiment

To assess the potential benefits from embedding the Dynamic Network Model into a short-term sepsis prediction system, the Latent Dynamics Model (see Section 5) was trained and evaluated using real-world medical data. This chapter presents the complete experimental setup, including the data basis (data source, cohort selection, preprocessing), the prediction task, and provide details on the implementation and training routine.

6.1. Data

This study relies exclusively on the Medical Information Mart for Intensive Care-IV database (version 2.3) [62]. The MIMIC database series contains EHR information capturing day-to-day clinical routines, including patient measurements, orders, diagnoses, procedures, treatments, and free-text clinical notes. All included EHRs were recorded at Beth Israel Deaconess Medical Center in Boston, America between 2008 and 2022. Every part of the data has been de-identified and is publicly available to support research in electronic healthcare applications, with special focus on intensive care. While applications trained on MIMIC databases are known to have limited generalization to other data-sources and real-world settings, they remain the default open-data resource for developing sepsis prediction systems [30], [63].

6.1.1. Cohort Definition, Feature Choice and Preprocessing

To derive the cohort from raw data and preprocess clinical features, the YAIB framework is used [34]. YAIB standardizes cohort definition, feature derivation and data preprocessing for retrospective ICU studies across different publicly available databases. It additionally provides benchmark results for common ICU prediction task, including the online prediction of sepsis. For this work, every step from the sepsis and cohort definition, feature choices to the data preprocessing, is adopted from their methodology [34] to enable direct comparison of prediction results.

Their definition closely follows the Sepsis-3 criteria [4]:

“ The onset of sepsis was defined using the Sepsis-3 criteria (Singer et al., 2016), which defines sepsis as organ dysfunction due to infection. Following guidance from the original authors of Sepsis-3 (Seymour et al., 2016), organ dysfunction was defined as an

increase in SOFA score ≥ 2 points compared to the lowest value over the last 24 hours. Suspicion of infection was defined as the simultaneous use of antibiotics and culture of body fluids. The time of sepsis onset was defined as the first time of organ dysfunction within 48 hours before and 24 hours after suspicion of infection. Time of suspicion was defined as the earlier antibiotic initiation or culture request. Antibiotics and culture were considered concomitant if the culture was requested ≤ 24 hours after antibiotic initiation or if antibiotics were started ≤ 72 hours after the culture was sent to the lab. Where available, antibiotic treatment was inferred from administration records; otherwise, we used prescription data. To exclude prophylactic antibiotics, we required that antibiotics were administered continuously for ≥ 3 days (Reyna et al., 2019). Antibiotic treatment was considered continuous if an antibiotic was administered once every 24 hours for 3 days (or until death) or was prescribed for the entire time spent in the ICU “

6.1.2. Cohort Selection

The cohort includes all adult patients (age at admission ≥ 18 , $N = 73,181$). To ensure data volume and quality, patients meeting any of the following criteria were excluded:

- Less than six hours spent in the ICU.
- Less than four separate hours across the entire stay where at least one feature was measured.
- Any time interval of ≥ 12 consecutive hours throughout the stay during which no feature was measured.
- Sepsis onset before the 6th hour in the ICU.

Applying these criteria resulted in a final cohort size of $N = 63,425$ patients. The selection process with corresponding exclusion numbers is shown in Figure 15.

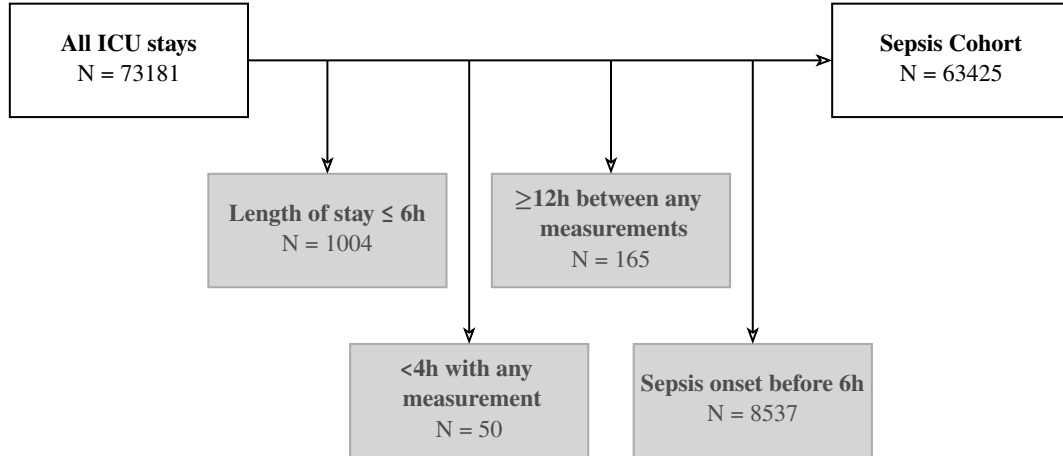


Figure 15: Cohort selection and exclusion process

6.1.3. Cohort Characteristics

Table 6 presents the demographic and clinical characteristics of the final cohort, stratified by sepsis status according to the Sepsis-3 criteria. Of the 63,425 patients included, 3,320 (5.2%) met criteria for sepsis. Sepsis-positive patients exhibited notably higher disease severity, with a median maximum SOFA score of 5.0 compared to 4.0 in sepsis-negative patients, and substantially higher hospital mortality (26.5% vs 6.6%). The median time to sepsis onset was 13.0 hours (Inter Quantile Range (IQR) (25%-75%): 8.0–34.0).

Both groups were similar in terms of demographic characteristics, including age (median 65 years), sex distribution (approximately 55% male), and weight at admission (median 77.6 kg). The majority of patients in both groups were white (63.6% overall) and had medical admissions (71.0% overall), though sepsis-positive patients had a higher proportion of medical admissions (84.8% vs 70.2%).

Table 6: Characteristics and demographics of the cohort. Numerical variables are summarized by *median [IQR 25 - 75]* and numerical variables by incidence (%)

CHARACTERISTIC	ALL PATIENTS	SEP-3 POSITIVE	SEP-3 NEGATIVE
N	63425 (100.0%)	3320 (5.2%)	60105 (94.8%)
Male	35170 (55.5%)	1881 (56.7%)	33289 (55.4%)
Age at admission	65.0 (53.0–76.0)	65.0 (54.0–76.0)	65.0 (53.0–76.0)
Weight at admission	77.6 (65.1–92.3)	77.6 (65.6–94.0)	77.6 (65.0–92.2)
Clinical Outcomes			
SOFA median	3.0 (1.0–5.0)	3.0 (1.0–5.0)	3.0 (1.0–5.0)
SOFA max	4.0 (2.0–6.0)	5.0 (4.0–8.0)	4.0 (2.0–6.0)
Hospital Length Of Stay (LOS) hours	157.7 (92.8–268.9)	335.1 (194.2–548.6)	150.3 (90.9–256.0)
Hospital Mortality	4828 (7.6%)	879 (26.5%)	3949 (6.6%)
SEP-3 onset time	-	13.0 (8.0–34.0)	-
Ethnicity			
White	40364 (63.6%)	2087 (62.9%)	38277 (63.7%)
Black	5809 (9.2%)	262 (7.9%)	5547 (9.2%)
Asian	721 (1.1%)	42 (1.3%)	679 (1.1%)
Hispanic	630 (1.0%)	32 (1.0%)	598 (1.0%)
Other/Unknown	14924 (23.5%)	897 (27.0%)	14027 (23.3%)
Admission Type			
Medical	45009 (71.0%)	2817 (84.8%)	42192 (70.2%)

CHARACTERISTIC	ALL PATIENTS	SEP-3 POSITIVE	SEP-3 NEGATIVE
Surgical	2239 (3.5%)	45 (1.4%)	2194 (3.7%)
Other/Unknown	15200 (24.0%)	458 (13.8%)	14742 (24.5%)

6.1.3.1. Feature Choice

To enable direct result comparisons with [34] benchmark, their feature set is adopted, which has been derived in collaboration with clinical experts. Each patient in the final cohort has 52 input-features, with four static (age, height, and weight at admission as well as sex) and 48 dynamic time-series variables. The dynamic variables combine seven vital signs and 39 laboratory tests, and two additional measurements (fraction of inspired oxygen and urine output). A complete listing of all features with their value ranges, units of measurement and clinical description is provided in Table 9.

The target variables include the SOFA-score, a SI label and the Sepsis-3 label (see Section 5.1).

6.1.3.2. Preprocessing

The data preprocessing involves three main steps: scaling, sampling, and imputation of features, which again were adopted from [34]. All numerical feature were standardized to zero mean and unit variance, while categorical and binary features remained left unchanged. To prevent data leakage, used statistics from the training split for all data partitions (training, validation, and testing) were used.

All features were uniformly resampled to an hourly basis. Missing data points for dynamic variables were forward-filled using the last known value of the same ICU stay. For missing values without any prior measurement, the training cohort mean is used as fill value instead. Lastly the data is augmented by a binary indicator that distinguishes between actual measurements and imputed values.

6.2. Implementation Details

The LDM was implemented in the JAX [51] based Equinox framework [64] and trained on a consumer laptop GPU. The cohort was partitioned at the patient level using a stratified split with a 75/12.5/12.5 ratio for training, validation, and test sets respectively. The split was stratified by sepsis status to maintain the 5.2% prevalence ratio across all sets. To address the strong imbalance between septic and non-septic samples, each training batch has been randomly oversampled to contain 10% positive samples.

All modules were jointly optimized using AdamW (learning rate = 3×10^{-3} , weight decay = 1×10^{-4}) with early stopping (patience= epochs on validation AUPRC). Batch size was 512 with [sequence handling details]. The DNM latent space was quantized to a 60×100 ...

grid over $\beta \in [0.4\pi, 0.7\pi]$ and $\sigma \in [0.0, 1.5]$, with differentiable lookup using 3x3 neighborhood softmax interpolation.

padding

Architecture specifications:

- The infection indicator module is a single single GRU cell with a hidden dimension of 16, followed by a linear down projection to the single target dimension.
- The SOFA pre-encoder uses [redacted], and the recurrent module a single GRU cell [redacted] with hidden dimension 4 followed by a linear down-projection to the 2 dimensional latent space.
- The decoder [redacted]

...
in methods?
... Loss weights were:

ask

6.3. Evaluation Metrics

The prediction of a patient developing sepsis vs. no sepsis is a binary decision problem based off of the continuous estimated heuristic sepsis risk S_t . Given an estimated risk S_t and a decision threshold $\tau \in [0, 1]$, the decision if a prediction value counts as septic is given by the rule:

$$\delta(\tilde{S}_t) = \mathbb{I}(\tilde{S}_t > \tau) \quad (6.51)$$

where $\mathbb{I}(\cdot)$ is 1 when the condition is met and 0 otherwise. For different choices of τ the decision rule can be applied and yield different ratios of:

- **True Positives (TP)** where truth and estimation are 1
- **False Positives (FP)** where truth is 0 and estimation 1
- **True Negatives (TN)** where truth and estimation are 0
- **False Negatives (FN)** where truth is 1 and estimation 0,

from these one can calculate the True Positive Rate (TPR) (also called sensitivity):

$$\text{TPR} = \frac{\text{TP}}{\text{TP} + \text{FN}} \quad (6.52)$$

and the False Positive Rate (FPR):

$$\text{FPR} = \frac{\text{FP}}{\text{TP} + \text{FN}} \quad (6.53)$$

Sweeping the decision boundary τ from 0 to 1 and plotting the corresponding implicit function TPR vs FPR creates the *receiver operating characteristic* or *ROC* curve. A prediction system operating at chance will have exhibit a diagonal line from (0 FPR, 0 TPR) to (1 FPR, 1 TPR). Everything above that diagonal indicates better predictions than chance, with an optimal predictor “hugging” the left axis until the point (0 FPR, 1 TPR) followed by hugging the top axis. The quality of the whole curve can be summarized to a single number,

the area under the curve, called AUROC, where larger values ≤ 1 indicate better prediction performance.

When trying to predict rare events, meaning sparse positive against lots of negative events the FPR can become small and thus little informative. In these cases one commonly plots the *precision*:

$$P = \frac{\text{TP}}{\text{TP} + \text{FP}} \quad (6.54)$$

against the *recall*:

$$R = \frac{\text{TP}}{\text{TP} + \text{FN}} \quad (6.55)$$

creating the *precision recall curve* or PRC, where an optimal predictor hugs the top right. Also this curve can be summarized by its area to the AUPRC metric, where larger values indicate better performance [65].

Traditionally, the AUPRC is referred to as the more appropriate metric for imbalanced prediction tasks. Though, recent research suggests the AUROC as a more reliable metric for use cases with elevated FN costs, such as the increased mortality risk in false or delayed sepsis diagnoses [66]. Together the AUROC and AUPRC are the commonly reported performance metrics used in the sepsis prediction literature [31] and will be used to compare the performance between the LDM and the YAIB baseline.

For binary decision problems such as the prediction of Model performance was evaluated using threshold-independent metrics appropriate for imbalanced binary classification:

- AUROC Measures discrimination ability across all classification thresholds
- AUPRC More informative than AUROC for imbalanced data, emphasizes performance on positive (sepsis) cases

All metrics were computed on the held-out test set. Statistical significance of performance differences was assessed using [bootstrapping / DeLong test / McNemar test].

6.4. Results and Benchmark Comparisons

7 Results

8 Conclusion

Appendix

A Appendix	61
A.1 SOFA - Details	61
A.2 DNM as Lie Formulation	62
A.3 Input Concepts	62

A Appendix

A.1 SOFA - Details

Table 7: TODO

CATEGORY	INDICATOR	1	2	3	4
Respiration	PaO ₂ /FiO ₂ [mmHg]	< 400	< 300	< 200	< 100
	Mechanical Ventilation			yes	yes
Coagulation	Platelets [$\times \frac{10^3}{\text{mm}^3}$]	< 150	< 100	< 50	< 20
Liver	Bilirubin [$\frac{\text{mg}}{\text{dl}}$]	1.2-1.9	2.0-5.9	6.0-11.9	> 12.0
Cardiovascular ⁴	MAP [mmHg]	< 70			
	or Dopamine		≤ 5	> 5	> 15
	or Dobutamine		any dose		
	or Epinephrine			≤ 0.1	> 0.1
	or Noepinephrine			≤ 0.1	> 0.1
Central Nervous System	Glasgow Coma Score	13-14	10-12	6-9	< 6
Renal	Creatinine [$\frac{\text{mg}}{\text{dl}}$]	1.2-1.9	2.0-3.4	3.5-4.9	> 5.0
	or Urine Output [$\frac{\text{ml}}{\text{day}}$]			< 500	< 200

⁴Adrenergic agents administered for at least 1h (doses given are in [$\mu\text{g}/\text{kg} \cdot \text{min}$])

A.2 DNM as Lie Formulation

A.3 Input Concepts

Table 8: Static input features for the prediction task

RICU - NAME	UNIT	MIN	MAX	DESCRIPTION
age	Years	0	-	Age at hospital admission
sex	-	-	-	Female Sex
height	kg	0	-	Patient height
weight	cm	0	-	Patient weight

Table 9: Dynamic input features for the prediction task.

RICU - NAME	UNIT	MIN	MAX	DESCRIPTION
alb	g/dL	0	6	albumin
alp	IU/L, U/l	0	-	alkaline phosphatase
alt	IU/L, U/l	0	-	alanine aminotransferase
ast	IU/L, U/l	0	-	aspartate aminotransferase
be	mEq/L, mmol/l	-25	25	base excess
bicar	mEq/L, mmol/l	5	50	bicarbonate
bili	mg/dL	0	100	total bilirubin
bili_dir	mg/dL	0	50	bilirubin direct
bnd	%	-	-	band form neutrophils
bun	mg/dL	0	200	blood urea nitrogen
ca	mg/dL	4	20	calcium
cai	mmol/L	0.5	2	calcium ionized
ck	IU/L, U/l	0	-	creatinine kinase
ckmb	ng/mL	0	-	creatinine kinase MB
cl	mEq/L, mmol/l	80	130	chloride
crea	mg/dL	0	15	creatinine
crp	mg/L	0	-	C-reactive protein
dbp	mmHg, mm Hg	0	200	diastolic blood pressure

fgn	mg/dL	0	1500	fibrinogen
fio2	%	21	100	fraction of inspired oxygen
glu	mg/dL	0	1000	glucose
hgb	g/dL	4	18	hemoglobin
hr	bpm, /min	0	300	heart rate
inr_pt	-	-	-	prothrombin time/international normalized ratio
k	mEq/L, mmol/l	0	10	potassium
lact	mmol/L	0	50	lactate
lymph	%	0	100	lymphocytes
map	mmHg, mm Hg	0	250	mean arterial pressure
mch	pg	0	-	mean cell hemoglobin
mchc	%	20	50	mean corpuscular hemoglobin concentration
mcv	fL	50	150	mean corpuscular volume
methb	%	0	100	methemoglobin
mg	mg/dL	0.5	5	magnesium
na	mEq/L, mmol/l	110	165	sodium
neut	%	0	100	neutrophils
o2sat	%, % Sat.	50	100	oxygen saturation
pco2	mmHg, mm Hg	10	150	CO2 partial pressure
ph	-	6.8	8	pH of blood
phos	mg/dL	0	40	phosphate
plt	K/uL, G/l	5	1200	platelet count
po2	mmHg, mm Hg	40	600	O2 partial pressure
ptt	sec	0	-	partial thromboplastin time
resp	insp/min, /min	0	120	respiratory rate
sbp	mmHg, mm Hg	0	300	systolic blood pressure
temp	C, °C	32	42	temperature
tnt	ng/mL	0	-	troponin t
urine	mL	0	2000	urine output

wbc	K/uL, G/l	0	-	white blood cell count
age	years	0	100	patient age
sex	-	-	-	patient sex
height	cm	10	230	patient height
weight	kg	1	500	patient weight

Bibliography

- [1] K. E. Rudd and et al., “Global, regional, and national sepsis incidence and mortality, 1990–2017: analysis for the Global Burden of Disease Study,” *The Lancet*, vol. 395, no. 10219, pp. 200–211, 2020, doi: 10.1016/S0140-6736(19)32989-7.
- [2] E. C. van der Slikke, A. Y. An, R. E. Hancock, and H. R. Bouma, “Exploring the pathophysiology of post-sepsis syndrome to identify therapeutic opportunities,” *EBioMedicine*, vol. 61, p. 103044, 2020, doi: 10.1016/j.ebiom.2020.103044.
- [3] C. Fleischmann-Struzek, D. Schwarzkopf, and K. Reinhart, “Inzidenz der Sepsis in Deutschland und weltweit: Aktueller Wissensstand und Limitationen der Erhebung in Abrechnungsdaten,” *Medizinische Klinik - Intensivmedizin und Notfallmedizin*, vol. 117, no. 4, pp. 264–268, May 2022, doi: 10.1007/s00063-021-00777-5.
- [4] M. Singer *et al.*, “The Third International Consensus Definitions for Sepsis and Septic Shock (Sepsis-3),” *JAMA*, vol. 315, no. 8, pp. 801–810, Feb. 2016, doi: 10.1001/jama.2016.0287.
- [5] Y. Chen and L. Tang, “The Crosstalk between Parenchymal Cells and Macrophages: A Keeper of Tissue Homeostasis,” *Frontiers in Immunology*, vol. 13, p. 1050188, 2022, doi: 10.3389/fimmu.2022.1050188.
- [6] A. M. Honan and Z. Chen, “Stromal Cells Underlining the Paths From Autoimmunity, Inflammation to Cancer With Roles Beyond Structural and Nutritional Support,” *Frontiers in Cell and Developmental Biology*, 2021, doi: 10.3389/fcell.2021.658984.
- [7] D. H. P. Directors, “Overview of Surface Epithelium.” [Online]. Available: <https://digitalhistology.org/tissues/epithelium/lining-and-covering/overview/overview-1/>
- [8] D. H. P. Directors, “Stroma and Parenchyma.” [Online]. Available: <https://digitalhistology.org/organs-systems/general-concepts/stroma-and-parenchyma/stroma-and-parenchyma-1/>
- [9] S. Fischer and E. Deindl, “State of the Art of Innate Immunity - An Overview,” *Cells*, vol. 11, p. 2705, 2022, doi: 10.3390/cells11172705.
- [10] D. Jarczak, S. Kluge, and A. Nierhaus, “Sepsis—Pathophysiology and Therapeutic Concepts,” *Frontiers in Medicine*, 2021, doi: 10.3389/fmed.2021.628302.
- [11] J. Zhang and J. An, “Cytokines, inflammation, and pain,” *Int Anesthesiol Clin*, vol. 45, no. 2, pp. 27–37, 2007, doi: 10.1097/AIA.0b013e318034194e.
- [12] R. V. House and J. Descotes, Eds., *Cytokines in Human Health: Immunotoxicology, Pathology, and Therapeutic Applications*, 1st ed. in Methods in Pharmacology and Toxicology. Totowa, N.J.: Humana Press, 2007.

- [13] D. Jarczak and A. Nierhaus, “Cytokine Storm—Definition, Causes, and Implications,” *International Journal of Molecular Sciences*, vol. 23, no. 19, 2022, doi: 10.3390/ijms231911740.
- [14] J. Lamsfus-Prieto, R. de Castro-Fernández, A. Hernández-García, and G. Marcano-Rodriguez, “Prognostic value of gasometric parameters of carbon dioxide in resuscitation of septic patients. A bibliography review,” *Revista Española de Anestesiología y Reanimación (English Edition)*, vol. 63, no. 4, pp. 220–230, 2016, doi: <https://doi.org/10.1016/j.redare.2015.11.003>.
- [15] J. L. Vincent *et al.*, “The SOFA (Sepsis-related Organ Failure Assessment) score to describe organ dysfunction/failure. On behalf of the Working Group on Sepsis-Related Problems of the European Society of Intensive Care Medicine,” *Intensive care medicine*, vol. 22, no. 7, pp. 707–710, 1996.
- [16] A. E. W. Johnson *et al.*, “A Comparative Analysis of Sepsis Identification Methods in an Electronic Database,” *Critical Care Medicine*, vol. 46, no. 4, pp. 494–499, Apr. 2018, doi: 10.1097/CCM.0000000000002965.
- [17] N. Bennett, D. Plečko, and I.-F. Ukor, “Sepsis 3 label — sep3.” 2025.
- [18] R. Moreno *et al.*, “The Sequential Organ Failure Assessment (SOFA) Score: has the time come for an update?,” *Critical Care*, vol. 27, no. 1, p. 15, Jan. 2023, doi: 10.1186/s13054-022-04290-9.
- [19] L. La Via *et al.*, “The Global Burden of Sepsis and Septic Shock,” *Epidemiologia*, vol. 5, no. 3, pp. 456–478, 2024, doi: 10.3390/epidemiologia5030032.
- [20] S. Ein Alshaeba, E. A. Marhoffer, J. L. Holleck, J. Theise-Toupal, A. A. Grimshaw, and C. G. Gunderson, “The Effect of Early Warning Systems for Sepsis on Mortality: A Systematic Review and Meta-analysis,” *Journal of General Internal Medicine (J GEN INTERN MED)*, vol. 40, pp. 3463–3468, 2025, doi: 10.1007/s11606-025-09569-5.
- [21] C. W. Seymour *et al.*, “Time to Treatment and Mortality during Mandated Emergency Care for Sepsis,” *The New England Journal of Medicine*, vol. 376, pp. 2235–2244, June 2017, doi: 10.1056/NEJMoa1703058.
- [22] G. A. Westphal *et al.*, “Early detection strategy and mortality reduction in severe sepsis,” *Revista Brasileira de Terapia Intensiva (Rev Bras Ter Intensiva)*, vol. 21, no. 2, pp. 113–123, June 2009.
- [23] G. P. Dobson, H. L. Letson, and J. L. Morris, “Revolution in sepsis: a symptoms-based to a systems-based approach?,” *Journal of Biomedical Science (J Biomed Sci)*, vol. 31, no. 1, p. 57, 2024, doi: 10.1186/s12929-024-01043-4.
- [24] B. Eini-Porat, O. Amir, D. Eytan, and U. Shalit, “Tell me something interesting: Clinical utility of machine learning prediction models in the ICU,” *Journal of Biomedical Informatics*, vol. 132, p. 104107, 2022, doi: 10.1016/j.jbi.2022.104107.
- [25] A. Schuurman, P. Sloot, W. Wiersinga, and et al., “Embracing complexity in sepsis,” *Crit Care*, vol. 27, no. 1, p. 102, 2023, doi: 10.1186/s13054-023-04374-0.
- [26] F. J. A. Relouw, M. Kox, H. R. Taal, B. C. P. Koch, M. W. J. Prins, and N. A. W. van Riel, “Mathematical model of the inflammatory response to acute and prolonged lipopolysaccharide exposure in humans,” *npj Systems Biology and Applications*, vol. 10, no. 1, p. 146, Dec. 2024, doi: 10.1038/s41540-024-00473-y.
- [27] G. An and C. Cockrell, “A design specification for Critical Illness Digital Twins to cure sepsis: responding to the National Academies of Sciences, Engineering and Medicine Report: Foundational Research Gaps and Future Directions for Digital Twins.” [Online]. Available: <https://arxiv.org/abs/2405.05301>
- [28] C. Cockrell, S. Schobel-McHugh, F. Lisboa, Y. Vodovotz, and G. An, “Generating synthetic data with a mechanism-based Critical Illness Digital Twin: Demonstration for Post Traumatic Acute Respiratory Distress Syndrome,” *bioRxiv*, 2023, doi: 10.1101/2022.11.22.517524.

- [29] M. McDaniel, J. M. Keller, S. White, and A. Baird, “A Whole-Body Mathematical Model of Sepsis Progression and Treatment Designed in the BioGears Physiology Engine,” *Frontiers in Physiology*, vol. 10, p. 1321, Oct. 2019, doi: 10.3389/fphys.2019.01321.
- [30] S. Bomrah *et al.*, “A scoping review of machine learning for sepsis prediction- feature engineering strategies and model performance: a step towards explainability,” *Critical Care*, vol. 28, no. 1, p. 180, May 2024, doi: 10.1186/s13054-024-04948-6.
- [31] M. Moor, B. Rieck, M. Horn, C. R. Jutzeler, and K. Borgwardt, “Early Prediction of Sepsis in the ICU Using Machine Learning: A Systematic Review,” *Frontiers in Medicine*, 2021, doi: 10.3389/fmed.2021.607952.
- [32] T. Chen and C. Guestrin, “XGBoost: A Scalable Tree Boosting System,” in *Proceedings of the 22nd ACM SIGKDD International Conference on Knowledge Discovery and Data Mining*, in KDD '16. San Francisco, California, USA: Association for Computing Machinery, 2016, pp. 785–794. doi: 10.1145/2939672.2939785.
- [33] M. Moor *et al.*, “Predicting sepsis using deep learning across international sites: a retrospective development and validation study,” *eClinicalMedicine*, vol. 62, p. 102124, 2023, doi: <https://doi.org/10.1016/j.eclim.2023.102124>.
- [34] R. van de Water, H. N. A. Schmidt, P. Elbers, P. Thoral, B. Arnrich, and P. Rockenschaub, “Yet Another ICU Benchmark: A Flexible Multi-Center Framework for Clinical ML,” in *The Twelfth International Conference on Learning Representations*, Oct. 2024.
- [35] R. E. Callard, A. J. T. George, and J. Stark, “Cytokines, chaos, and complexity,” *Immunity*, vol. 11, no. 5, pp. 507–513, Nov. 1999, doi: 10.1016/s1074-7613(00)80125-9.
- [36] P. C. Ivanov, “The New Field of Network Physiology: Building the Human Physiolome,” *Frontiers in Network Physiology*, 2021, doi: 10.3389/fnetp.2021.711778.
- [37] A. C. Guyton, T. G. Coleman, and H. J. Granger, “Circulation: overall regulation,” *Annu Rev Physiol*, vol. 34, pp. 13–46, 1972, doi: 10.1146/annurev.ph.34.030172.000305.
- [38] R. P. Bartsch, A. Y. Schumann, J. W. Kantelhardt, T. Penzel, and P. C. Ivanov, “Phase transitions in physiologic coupling,” *Proc Natl Acad Sci U S A*, vol. 109, no. 26, pp. 10181–10186, June 2012, doi: 10.1073/pnas.1204568109.
- [39] K. Lehnertz, T. Rings, and T. Bröhl, “Time in Brain: How Biological Rhythms Impact on EEG Signals and on EEG-Derived Brain Networks,” *Front. Netw. Physiol.*, vol. 1, p. 755016, Sept. 2021, doi: 10.3389/fnetp.2021.755016.
- [40] M. Madadi Asl, A.-H. Vahabie, A. Valizadeh, and P. A. Tass, “Spike-Timing-Dependent Plasticity Mediated by Dopamine and its Role in Parkinson’s Disease Pathophysiology,” *Frontiers in Network Physiology*, 2022, doi: 10.3389/fnetp.2022.817524.
- [41] N. Sinha, R. B. Joshi, M. R. S. Sandhu, T. I. Netoff, H. P. Zaveri, and K. Lehnertz, “Perspectives on Understanding Aberrant Brain Networks in Epilepsy,” *Frontiers in Network Physiology*, 2022, doi: 10.3389/fnetp.2022.868092.
- [42] J. Sawicki, R. Berner, T. Löser, and E. Schöll, “Modeling Tumor Disease and Sepsis by Networks of Adaptively Coupled Phase Oscillators,” *Frontiers in Network Physiology*, vol. 1, 2022, doi: 10.3389/fnetp.2021.730385.
- [43] R. Berner, J. Sawicki, M. Thiele, T. Löser, and E. Schöll, “Critical Parameters in Dynamic Network Modeling of Sepsis,” *Frontiers in Network Physiology*, vol. 2, 2022, doi: 10.3389/fnetp.2022.904480.
- [44] A. Pikovsky, M. Rosenblum, and J. Kurths, *Synchronization: A Universal Concept in Nonlinear Sciences*, vol. 12. Cambridge University Press, 2001.
- [45] Y. Kuramoto, *Chemical Oscillations, Waves, and Turbulence*, vol. 19. Berlin, Heidelberg: Springer-Verlag, 1984.

- [46] J. A. Acebrón, L. L. Bonilla, C. J. Pérez Vicente, F. Ritort, and R. Spigler, “The Kuramoto model: A simple paradigm for synchronization phenomena,” *Reviews of Modern Physics*, vol. 77, no. 1, pp. 137–185, 2005.
- [47] H. Sakaguchi and Y. Kuramoto, “A Soluble Active Rotator Model Showing Phase Transitions via Mutual Entrainment,” *Progress of Theoretical Physics*, vol. 76, no. 3, pp. 576–581, 1986, doi: 10.1143/PTP.76.576.
- [48] R. Berner, J. Sawicki, and E. Schöll, “Birth and Stabilization of Phase Clusters by Multiplexing of Adaptive Networks,” *Phys. Rev. Lett.*, vol. 124, no. 8, p. 88301, Feb. 2020, doi: 10.1103/PhysRevLett.124.088301.
- [49] Max, “Placeholder.”
- [50] R. Berner, J. Fialkowski, D. Kasatkin, V. Nekorkin, S. Yanchuk, and E. Schöll, “Hierarchical frequency clusters in adaptive networks of phase oscillators,” *Chaos: An Interdisciplinary Journal of Nonlinear Science*, vol. 29, no. 10, p. 103134, 2019, doi: 10.1063/1.5097835.
- [51] J. Bradbury *et al.*, “JAX: composable transformations of Python+NumPy programs.” [Online]. Available: <http://github.com/jax-ml/jax>
- [52] P. Kidger, “On Neural Differential Equations,” Doctoral dissertation, 2021.
- [53] C. Tsitouras, “Runge–Kutta pairs of order 5 (4) satisfying only the first column simplifying assumption,” *Computers & Mathematics with Applications*, vol. 62, no. 2, pp. 770–775, 2011.
- [54] T. Böhle, C. Kuehn, and M. Thalhammer, “On the reliable and efficient numerical integration of the Kuramoto model and related dynamical systems on graphs,” *International Journal of Computer Mathematics*, vol. 99, no. 1, pp. 31–57, 2022, doi: 10.1080/00207160.2021.1952997.
- [55] Y. Bengio, N. Léonard, and A. Courville, “Estimating or Propagating Gradients Through Stochastic Neurons for Conditional Computation.” [Online]. Available: <https://arxiv.org/abs/1308.3432>
- [56] F. Mentzer, D. Minnen, E. Agustsson, and M. Tschannen, “Finite Scalar Quantization: VQ-VAE Made Simple.” [Online]. Available: <https://arxiv.org/abs/2309.15505>
- [57] D. Hafner, J. Pasukonis, J. Ba, and T. Lillicrap, “Mastering Diverse Domains through World Models.” [Online]. Available: <https://arxiv.org/abs/2301.04104>
- [58] P. Kidger, “On Neural Differential Equations.” [Online]. Available: <https://arxiv.org/abs/2202.02435>
- [59] A. A. Sophiya, A. K. Nair, S. Maleki, and S. K. Krishnababu, “A comprehensive analysis of PINNs: Variants, Applications, and Challenges.” [Online]. Available: <https://arxiv.org/abs/2505.22761>
- [60] Y. Bengio, A. C. Courville, and P. Vincent, “Representation Learning: A Review and New Perspectives,” *CoRR*, 2012, [Online]. Available: <http://arxiv.org/abs/1206.5538>
- [61] T.-Y. Lin, P. Goyal, R. Girshick, K. He, and P. Dollár, “Focal Loss for Dense Object Detection.” [Online]. Available: <https://arxiv.org/abs/1708.02002>
- [62] A. E. W. Johnson and others, “MIMIC-IV, a freely accessible electronic health record dataset,” *Scientific Data*, vol. 10, no. 1, p. 1, Jan. 2023, doi: 10.1038/s41597-022-01899-x.
- [63] P. Rockenschaub *et al.*, “Generalisability of AI-based scoring systems in the ICU: a systematic review and meta-analysis,” *medRxiv*, 2023, doi: 10.1101/2023.10.11.23296733.
- [64] P. Kidger and C. Garcia, “Equinox: neural networks in JAX via callable PyTrees and filtered transformations,” *Differentiable Programming workshop at Neural Information Processing Systems 2021*, 2021.
- [65] K. P. Murphy, *Machine Learning: A Probabilistic Perspective*. Cambridge, MA: MIT Press, 2012.
- [66] M. B. A. McDermott, H. Zhang, L. H. Hansen, G. Angelotti, and J. Gallifant, “A Closer Look at AUROC and AUPRC under Class Imbalance.” [Online]. Available: <https://arxiv.org/abs/2401.06091>